

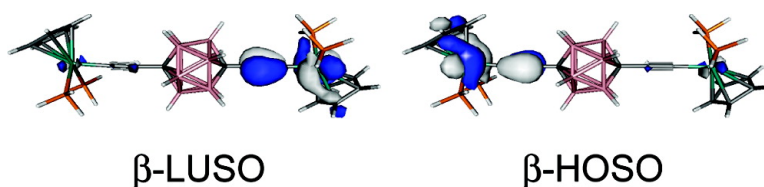
Article

Ruthenium Complexes of C,C'-Bis(ethynyl)carboranes: An Investigation of Electronic Interactions Mediated by Spherical Pseudo-aromatic Spacers

Mark A. Fox, Rachel L. Roberts, Thomas E. Baines, Boris Le Guennic, Jean-Francois Halet, Frantiek Hartl, Dmitri S. Yufit, David Albesa-Jov, Judith A. K. Howard, and Paul J. Low

J. Am. Chem. Soc., **2008**, 130 (11), 3566-3578 • DOI: 10.1021/ja0779755

Downloaded from <http://pubs.acs.org> on February 8, 2009



More About This Article

Additional resources and features associated with this article are available within the HTML version:

- Supporting Information
- Links to the 1 articles that cite this article, as of the time of this article download
- Access to high resolution figures
- Links to articles and content related to this article
- Copyright permission to reproduce figures and/or text from this article

[View the Full Text HTML](#)

Ruthenium Complexes of C,C'-Bis(ethynyl)carboranes: An Investigation of Electronic Interactions Mediated by Spherical Pseudo-aromatic Spacers

Mark A. Fox,[†] Rachel L. Roberts,[†] Thomas E. Baines,[†] Boris Le Guennic,^{‡,§}
Jean-François Halet,[‡] František Hartl,^{||} Dmitri S. Yufit,[†] David Albesa-Jové,[†]
Judith A. K. Howard,[†] and Paul J. Low^{*,†}

Department of Chemistry, Durham University, South Rd, Durham, DH1 3LE, UK, Laboratoire des Sciences Chimiques de Rennes, UMR 6226 CNRS-Université de Rennes 1, 35042 Rennes cedex, France, Laboratoire de Chimie, UMR CNRS 5182, Ecole Normale Supérieure de Lyon, 46 allée d'Italie, 69364 Lyon cedex 07, France, and Van 't Hoff Institute for Molecular Sciences, University of Amsterdam, Nieuwe Achtergracht 166, 1018WW Amsterdam, The Netherlands

Received October 17, 2007; E-mail: p.j.low@durham.ac.uk

Abstract: The complexes [Ru(1-C≡C-1,10-C₂B₈H₉)(dppe)Cp*] (**3a**), [Ru(1-C≡C-1,12-C₂B₁₀H₁₁)(dppe)Cp*] (**3b**), [{"Ru(dppe)Cp*}₂{μ-1,10-(C≡C)₂-1,10-C₂B₈H₈}] (**4a**) and [{"Ru(dppe)Cp*}₂{μ-1,12-(C≡C)₂-1,12-C₂B₁₀H₁₀}] (**4b**), which form a representative series of mono- and bimetallic acetylide complexes featuring 10- and 12-vertex carboranes embedded within the diethynyl bridging ligand, have been prepared and structurally characterized. In addition, these compounds have been examined spectroscopically (UV-vis-NIR, IR) in all accessible redox states. The significant separation of the two, one-electron anodic waves observed in the cyclic voltammograms of the bimetallic complexes **4a** and **4b** is largely independent of the nature of the electrolyte and is attributed to stabilization of the intermediate redox products [**4a**]⁺ and [**4b**]⁺ through interactions between the metal centers across a distance of ca. 12.5 Å. The mono-oxidized bimetallic complexes [**4a**]⁺ and [**4b**]⁺ exhibit spectroscopic properties consistent with a description of these species in terms of valence-localized (class II) mixed-valence compounds, including a unique low-energy electronic absorption band, attributed to an IVCT-type transition that tails into the IR region. DFT calculations with model systems [**4a-H**]⁺ and [**4b-H**]⁺ featuring simplified ligand sets reproduce the observed spectroscopic data and localized electronic structures for the mixed-valence cations [**4a**]⁺ and [**4b**]⁺.

Introduction

The study of bridge-mediated electronic interactions between organic, organometallic and inorganic probe groups has been spurred by interest in the fundamentals of the electron (or hole)-transfer process,¹ and the prospect of using such systems in the construction of the highly functionalized molecules necessary for the realization of molecular electronic devices.² The ethynyl moiety, which offers a linear geometry, polarizable π-electron system and cylindrical symmetry, is often incorporated into the

bridge structures and many bimetallic complexes featuring, for example, diethynyl aromatic³ and polyynidyl⁴ bridging ligands are now known.

[†] Durham University.

[‡] UMR 6226 CNRS-Université de Rennes 1.

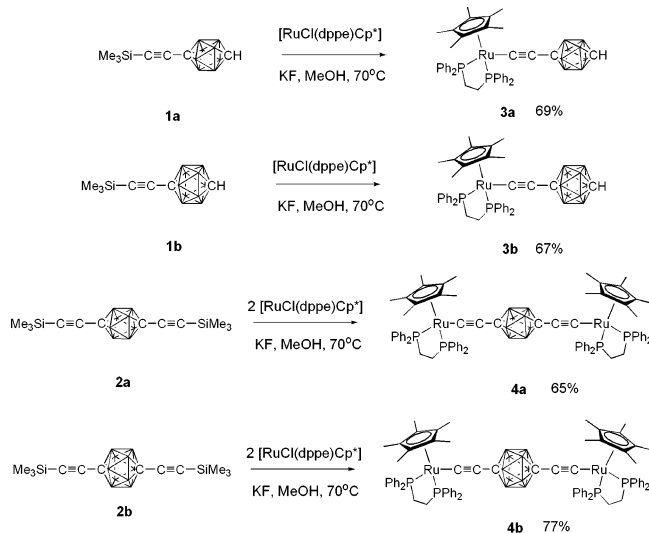
[§] UMR CNRS 5182, Ecole Normale Supérieure de Lyon.

^{||} University of Amsterdam.

- (1) (a) Brunshwig, B. S.; Creutz, C.; Sutin, N. *Coord. Chem. Rev.* **1998**, *177*, 61. (b) Creutz, C. *Prog. Inorg. Chem.* **1983**, *30*, 1. (c) Lambert, C.; Risko, C.; Coropceanu, V.; Shelter, J.; Amthor, S.; Gruhn, N. E.; Durivage, J. C.; Bredas, J. L. *J. Am. Chem. Soc.* **2005**, *127*, 8508. (d) Lambert, C.; Amthor, S.; Schelter, J. *J. Phys. Chem. A* **2004**, *108*, 6474. (e) Karafiloglou, P.; Launay, J.-P. *Chem. Phys.* **2003**, *289*, 231. (f) Launay, J.-P. *Chem. Soc. Rev.* **2001**, *30*, 386.
- (2) (a) Adams, D. M.; et al. *J. Phys. Chem. B* **2003**, *107*, 6668. (b) Low, P. J. *Dalton Trans.* **2005**, 2821. (c) Ren, T. *Organometallics* **2005**, *24*, 4854. (d) Benniston, A. C. *Chem. Soc. Rev.* **2004**, *33*, 573. (e) Coe, B. J.; Curati, N. R. M. *Comments Inorg. Chem.* **2004**, *25*, 147. (f) Carroll, R. L.; Gorman, C. B. *Angew. Chem., Int. Ed.* **2002**, *41*, 4379. (g) Astruc, D. *Acc. Chem. Res.* **1997**, *30*, 383.

- (3) For a selection of examples of this burgeoning field see: (a) Field, L. D.; George, A. V.; Laschi, F.; Malouf, E. Y.; Zanello, P. *J. Organomet. Chem.* **1992**, *435*, 347. (b) Khan, M. S.; Kakkur, A. K.; Ingham, S. L.; Raithby, P. R.; Lewis, J.; Spencer, B.; Wittmann, F.; Friend, R. H. *J. Organomet. Chem.* **1994**, *472*, 247. (c) Faulkner, C. W.; Ingham, S. L.; Khan, M. S.; Lewis, J.; Long, N. J.; Raithby, P. R. *J. Organomet. Chem.* **1994**, *482*, 139. (d) Le Narvor, N.; Lapinte, C. *Organometallics* **1995**, *14*, 634. (e) Lavastre, O.; Plass, J.; Bachmann, P.; Guesmi, S.; Moinet, C.; Dixneuf, P. H. *Organometallics* **1997**, *16*, 184. (f) Paul, F.; Lapinte, C. *Coord. Chem. Rev.* **1998**, *178–180*, 431. (g) Bruce, M. I.; Hall, B. C.; Low, P. J.; Skelton, B. W.; White, A. H. *J. Organomet. Chem.* **1999**, *592*, 74. (h) Albertin, G.; Antoniutti, S.; Bordignon, E.; Granzotto, M. *J. Organomet. Chem.* **1999**, *585*, 83. (i) Albertin, G.; Antoniutti, S.; Bordignon, E.; Bresolin, D. *J. Organomet. Chem.* **2000**, *609*, 10. (j) Weyland, T.; Ledoux, I.; Brasselet, S.; Zyss, J.; Lapinte, C. *Organometallics* **2000**, *19*, 5235. (k) Werner, H.; Bachmann, P.; Martin, M. *Can. J. Chem.* **2001**, *79*, 519. (l) Hurst, S. K.; Ren, T. *J. Organomet. Chem.* **2002**, *660*, 1. (m) Long, N. J.; Williams, C. K. *Angew. Chem., Int. Ed.* **2003**, *42*, 2586. (n) Wong, K. M. C.; Lam, S. C. F.; Ko, C. C.; Zhu, N. Y.; Yam, V. W. W.; Roue, S.; Lapinte, C.; Fathallah, S.; Costuas, K.; Kahlal, S.; Halet, J.-F. *Inorg. Chem.* **2003**, *42*, 7086. (o) Yam, V. W. W. *J. Organomet. Chem.* **2004**, *689*, 1393. (p) Saha, R.; Qaium, Md. A.; Debnath, D.; Younis, M.; Chawdhury, N.; Sultana, N.; Kociok-Kohn, G.; Ooi, L.; Raithby, P. R.; Kijima, M. *Dalton Trans.* **2005**, 2760. (q) de Montigny, F.; Argouarch, G.; Costuas, K.; Halet, J.-F.; Roisnel, T.; Toupet, L.; Lapinte, C. *Organometallics* **2005**, *24*, 4558. (r) Low, P. J.; Roberts, R. L.; Cordiner, R. L.; Hartl, F. *J. Solid State Electrochem.* **2005**, *9*, 717.
- (4) Bruce, M. I.; Low, P. J. *Adv. Organomet. Chem.* **2004**, *50*, 179.

Scheme 1. Preparation of Monoruthenium (**3a**, **3b**) and Diruthenium Complexes (**4a**, **4b**) via In Situ Metalation/Desilylation Reactions



The intriguing possibilities that arise from combination of the ethynyl moiety with the interesting and potentially useful physical and electronic properties offered by the *p*-carboranyl moiety, such as high symmetry along the $C\cdots C$ axis, high thermal and chemical stability, and spherical or “three-dimensional” aromaticity,⁵ has sparked considerable interest in the use of diethynylcarborane-based ligands as structural elements in multimetallic assemblies.⁶ This interest can only be expected to increase now that convenient synthetic routes to 10- and 12-vertex diethynyl-*p*-carboranes 1,10-($Me_3SiC\equiv C$)₂-1,10- $C_2B_8H_8$ (**2a**) and 1,12-($Me_3SiC\equiv C$)₂-1,12- $C_2B_{10}H_{10}$ (**2b**) have been reported (Scheme 1).^{7–12} The rigid geometry of the diethynyl carboranes together with the potential for the *p*-carborane cage to mediate electronic effects between groups located at the 1 and 10 (**2a**) or 1 and 12 (**2b**) positions has prompted consideration of diethynyl carboranes as conduits for electronic interactions between remote metal centers.¹³ Indeed, on the basis of computational results, it has been suggested that the degree of electronic communication between the apical substituents of the 10-vertex carborane cage may be comparable to that of *para*-substituted benzenes.¹¹ Hawthorne’s group

reported the first experimental steps in this area and described the preparation and electrochemical properties of $\{[Fe(CO)_2Cp]_2-(\mu-1,12-(C\equiv C)_2-1,12-C_2B_{10}H_{10})]\}^+$.¹⁴ Unfortunately, the limited thermodynamic stability of the mono-oxidized derivative $\{[Fe(CO)_2Cp]_2(\mu-1,12-(C\equiv C)_2-1,12-C_2B_{10}H_{10})\}^+$ with respect to disproportionation hampered efforts to probe this interesting species more thoroughly.

Half-sandwich complexes with supporting phosphine ligands have proven to be particularly useful probe groups in studies of bimetallic systems featuring ethynyl-based bridging ligands, often giving rise to radical derivatives with appreciable chemical and thermodynamic stability.¹⁵ With this in mind, we have prepared the complexes $[Ru(1-C\equiv C-1,10-C_2B_8H_9)(dppe)Cp^*]$ (**3a**), $[Ru(1-C\equiv C-1,12-C_2B_{10}H_{11})(dppe)Cp^*]$ (**3b**), $\{[Ru(dppe)Cp^*]_2\{\mu-1,10-(C\equiv C)_2-1,10-C_2B_8H_8\}\}$ (**4a**) and $\{[Ru(dppe)Cp^*]_2\{\mu-1,12-(C\equiv C)_2-1,12-C_2B_{10}H_{10}\}\}$ (**4b**), which form a representative series of mono- and bimetallic acetylide complexes featuring 10- and 12-vertex carboranes embedded within the diethynyl bridging ligand. We have used these systems to address the role of the polyhedral *p*-carborane cages in promoting electronic interactions between remote sites, the nature of the formally mixed-valence compounds that may be derived from them, and a DFT-based study of the electronic structure in each of the electrochemically accessible redox states.

Results and Discussion

Syntheses. Acetylide complexes of half-sandwich group 8 bis(phosphine) fragments such as $Ru(dppe)Cp^*$ are conveniently prepared from terminal acetylenes, via intermediate vinylidenes,^{16,17} or by fluoride-induced desilylmetalation of trimethylsilyl-protected acetylenes.^{18,19} The parent mono- and diethynyl carboranes are highly volatile,^{7–9} and so for convenience the trimethylsilyl derivatives 1- $Me_3SiC\equiv C-1,10-C_2B_8H_9$ (**1a**), prepared by copper(I)-mediated cross-coupling of $BrC\equiv CSiMe_3$ with 1,10- $C_2B_8H_{10}$,⁹ 1- $Me_3SiC\equiv C-1,12-C_2B_{10}H_{11}$ (**1b**),⁹ 1,10-($Me_3SiC\equiv C$)₂-1,10- $C_2B_8H_8$ (**2a**)⁷ and 1,12-($Me_3SiC\equiv C$)₂-1,12- $C_2B_{10}H_{10}$ (**2b**)⁷ were used in the preparation of complexes **3a**, **3b**, **4a** and **4b**, respectively (Scheme 1).

The ruthenium complexes **3a**, **3b**, **4a** and **4b** were characterized by the usual spectroscopic methods and single-crystal X-ray diffraction. The phosphine ligands gave rise to singlet resonances in the ³¹P NMR spectra near 81.6 ppm, which compare well

- (5) (a) Aihara, J. *J. Am. Chem. Soc.* **1978**, *100*, 3339. (b) Schleyer, P. v. R.; Maerker, C.; Dransfield, A.; Jiao, H.; Hommes, N. J. R. v. E. *J. Am. Chem. Soc.* **1996**, *118*, 6317.
- (6) (a) Vicente, J.; Chicote, M.-T.; Alvarez-Falcón, M. M.; Fox, M. A.; Bautista, D. *Organometallics* **2003**, *22*, 4792. (b) Jude, H.; Disteldorf, H.; Fischer, S.; Wedge, T.; Hawkridge, A. M.; Arif, A. M.; Hawthorne, M. F.; Muddiman, D. C.; Stang, P. J. *J. Am. Chem. Soc.* **2005**, *127*, 12131.
- (7) Fox, M. A.; Baines, T. E.; Albesa-Jové, D.; Howard, J. A. K.; Low, P. J. *J. Organomet. Chem.* **2006**, *691*, 3889.
- (8) Batsanov, A. S.; Fox, M. A.; Howard, J. A. K.; MacBride, J. A. H.; Wade, K. J. *Organomet. Chem.* **2000**, *610*, 20.
- (9) Fox, M. A.; Cameron, A. M.; Low, P. J.; Paterson, M. A. J.; Batsanov, A. S.; Goeta, A. E.; Rankin, D. W. H.; Robertson, H. E.; Schirlin, J. T. *Dalton Trans.* **2006**, 3544.
- (10) Kaszynski, P.; Pakhomov, S.; Young, V. G., Jr. *Collect. Czech. Chem. Commun.* **2002**, *67*, 1061.
- (11) Pakhomov, S.; Kaszynski, P.; Young, V. G., Jr. *Inorg. Chem.* **2000**, *39*, 2243.
- (12) Herzog, A.; Jalisatgi, S. S.; Knobler, C. B.; Wedge, T. J.; Hawthorne, M. F. *Chem. Eur. J.* **2005**, *11*, 7155.
- (13) (a) Fox, M. A.; MacBride, J. A. H.; Peace, R. J.; Wade, K. J. *Chem. Soc., Dalton Trans.* **1998**, 401. (b) Allis, D. G.; Spencer, J. T. *Inorg. Chem.* **2001**, *40*, 3373. (c) Allis, D. G.; Spencer, J. T. *J. Organomet. Chem.* **2000**, *614–615*, 309. (d) Fox, M. A.; Paterson, M. A. J.; Nervi, C.; Galeotti, F.; Puschmann, H.; Howard, J. A. K.; Low, P. J. *Chem. Commun.* **2001**, 1610. (e) Le Guennic, B.; Costuas, K.; Halet, J.-F.; Nervi, C.; Paterson, M. A. J.; Fox, M. A.; Roberts, R. L.; Albesa-Jové, D.; Puschmann, H.; Howard, J. A. K.; Low, P. J. *C. R. Chimie* **2005**, *8*, 1883.

- (14) Wedge, T. J.; Herzog, A.; Huertas, R.; Lee, M. W.; Knobler, C. B.; Hawthorne, M. F. *Organometallics* **2004**, *23*, 482.
- (15) (a) Cordiner, R. L.; Feroze, M. P.; Albesa-Jové, D.; Yufit, D. S.; Howard, J. A. K.; Low, P. J. *Inorg. Chim. Acta* **2006**, *359*, 3459. (b) Bruce, M. I.; Low, P. J.; Hartl, F.; Humphrey, P. A.; de Montigny, F.; Jevric, M.; Lapinte, C.; Perkins, G. J.; Roberts, R. L.; Skelton, B. W.; White, A. H. *Organometallics* **2005**, *24*, 5241. (c) Bruce, M. I.; Costuas, K.; Davin, T.; Ellis, B. G.; Halet, J.-F.; Lapinte, C.; Low, P. J.; Smith, M. E.; Skelton, B. W.; Toupet, L.; White, A. H. *Organometallics* **2005**, *24*, 3864. (d) Bruce, M. I.; Low, P. J.; Costuas, K.; Halet, J.-F.; Best, S. P.; Heath, G. A. *J. Am. Chem. Soc.* **2000**, *122*, 1949. (e) Jiao, H. J.; Costuas, K.; Gladysz, J. A.; Halet, J.-F.; Guillemot, M.; Toupet, L.; Paul, F.; Lapinte, C. *J. Am. Chem. Soc.* **2003**, *125*, 9511. (f) Paul, F.; Meyer, W. E.; Toupet, L.; Jiao, H. J.; Gladysz, J. A.; Lapinte, C. *J. Am. Chem. Soc.* **2000**, *122*, 9405. (g) Dembinski, R.; Bartik, T.; Bartik, B.; Jaeger, M.; Gladysz, J. A. *J. Am. Chem. Soc.* **2000**, *122*, 810. (h) Paul, F.; Lapinte, C. *Coord. Chem. Rev.* **1998**, *178*, 431.
- (16) Paul, F.; Ellis, B. G.; Bruce, M. I.; Toupet, L.; Roisnel, T.; Costuas, K.; Halet, J.-F.; Lapinte, C. *Organometallics* **2006**, *25*, 649.
- (17) Bitcon, C.; Whiteley, M. W. *J. Organomet. Chem.* **1987**, *336*, 385.
- (18) Bruce, M. I.; Hall, B. C.; Kelly, B. D.; Low, P. J.; Skelton, B. W.; White, A. H. *J. Chem. Soc., Dalton Trans.* **1999**, 3719.
- (19) (a) Bruce, M. I.; Kelly, B. D.; Skelton, B. W.; White, A. H. *J. Organomet. Chem.* **2000**, *604*, 150. (b) Coat, F.; Thomnot, P.; Lapinte, C. *J. Organomet. Chem.* **2001**, *629*, 39. (c) Bruce, M. I.; de Montigny, F.; Jevric, M.; Lapinte, C.; Skelton, B. W.; Smith, M. E.; White, A. H. *J. Organomet. Chem.* **2004**, *689*, 2860.

Table 1. Selected NMR Spectroscopic Data for Compounds and Complexes 1,10-R,R'-1,10-C₂B₈H₈

R	R'		C1 ^a	C10	C10H	B2-5	B6-9	B2-5H	B6-9H
H	H		101.7		7.00	-12.7		2.00	
Me ₃ SiCC	H	1a	104.1	98.3	6.85	-9.3	-13.3	2.31	2.03
Cp*(dppf)RuCC	H	3a	117.8	82.8	6.01	-11.3	-15.7	1.66	1.83
C ₂ B ₈ H ₉	H		120.5	97.8	7.01	-8.8	-12.8	2.56	2.18
HCC	HCC		99.8			-9.8		2.35	
Me ₃ SiCC	Me ₃ SiCC	2a	100.7			-10.0		2.30	
Cp*(dppe)RuCC	Cp*(dppe)RuCC	4a	99.3			-13.4		1.70	

^a See Figures 1–5 for atom labeling schemes used in this and all other tables.

Table 2. Selected NMR Spectroscopic Data for Compounds and Complexes 1,12-R,R'-1,12-C₂B₁₀H₁₀

R	R'		C1	C12	C12H	B2-6	B7-11	B2-6H	B7-11H
H	H		63.5		2.74	-14.9		2.10	
HCC	H		67.9	60.4	2.61	-11.6	-15.1	2.41	2.16
Me ₃ SiCC	H	1b	69.6	59.9	2.61	-11.5	-15.2	2.44	2.22
Cp*(dppe)RuCC	H	3b	78.7	53.4	2.28	-11.1	-16.3	1.82	2.14
HCC	HCC		65.3			-11.9		2.49	
Me ₃ SiCC	Me ₃ SiCC	2b	66.0			-11.9		2.44	
Cp*(dppe)RuCC	Cp*(dppe)RuCC	4b	69.3			-12.2		1.96	

Table 3. Selected Bond Lengths (Å) and Angles (deg) Associated with **1a**, **1b**, **2a**, **2b**, **3a**, **3b**, **4a** and **4b**

	1a	1b ^a	2a ^{c11}	2b ^a	3a	3b ^b (A)	3b ^b (B)	4a ^d	4b ^c
Si(1)–C(3)	1.847(2)	1.840(5)	1.848(2), 1.845(2)	1.856(2)					
Ru(1)–C(3)					1.999(2)	2.003(2)	2.004(2)	2.000(3)	1.991(4)
Ru(1)–P(1)					2.2745(6)	2.2620(4)	2.2463(4)	2.2548(7)	2.2509(10)
Ru(1)–P(2)					2.2587(7)	2.2602(4)	2.2656(4)	2.2738(7)	2.2638(11)
C(2)–C(3)	1.197(3)	1.227(5)	1.199(2), 1.200(3)	1.204(2)	1.214(3)	1.212(2)	1.217(2)	1.213(4)	1.205(4)
C(1)–C(2)	1.436(3)	1.442(5)	1.439(2), 1.434(2)	1.453(2)	1.443(3)	1.437(2)	1.440(2)	1.427(4)	1.454(5)
C(1)–B(2-5/6)	1.611(3)	1.725(6)	1.614(3)	1.728(2)	1.619(3)	1.721(3)	1.731(4)	1.623(5)	1.726(6)
B(2)–B(3)	1.853(3)	1.789(6)	1.856(3)	1.793(3)	1.846(4)	1.775(6)	1.784(4)	1.846(5)	1.774(6)
B(2)–B(6/7)	1.810(3)	1.765(8)	1.809(3)	1.769(2)	1.808(4)	1.757(6)	1.764(4)	1.802(5)	1.756(6)
B(6/7-7/8)	1.850(4)	1.792(7)	1.854(3)		1.844(4)	1.770(9)	1.779(4)	1.843(5)	
C(10/12)–B	1.597(4)	1.708(7)	1.614(3)		1.595(4)	1.696(6)	1.707(4)	1.621(4)	
Si(1)/Ru(1)–C(3)–C(2)	176.6(2)	180.0	177.1(2), 175.2(2)	177.9(2)	172.6(2)	176.6(2)	172.6(2)	173.9(3)	172.4(3)
C(1)–C(2)–C(3)	179.4(2)	180.0	178.1(2), 177.1(2)	179.4(2)	169.9(2)	176.0(2)	173.3(2)	175.3(3)	171.8(4)
P(1)–Ru(1)–P(2)					83.61(2)	81.16(2)	82.45(2)	83.30(3)	83.52(4)
Ru(1)···Ru(2)								12.643	12.373

^a Gas-phase electron diffraction. ^b Two independent molecules in the unit cell. ^c Molecule in a special position at the center of symmetry. ^d Also Ru(2)–C(5) 1.999(3) Å, Ru(2)–P(3) 2.2732(8) Å, Ru(2)–P(4) 2.2716(7) Å, C(5)–C(4) 1.215(4) Å, C(4)–C(10) 1.435(4) Å, Ru(2)–C(5)–C(4) 172.9(3)°, C(5)–C(4)–C(10) 174.9(3)°, P(3)–Ru(2)–P(4) 83.12(3)°.

with the values found for other acetylide complexes of this metal fragment.¹⁶ In the ¹³C NMR spectrum, resonances from the acetylide carbons were detected near 100 and 120 ppm, attributed to C(3) and C(2), respectively, on the basis of the *J*_{CP} coupling constants (ca. 25 Hz) associated with C(3) (Table 1).

Tables 1 and 2 list additional NMR spectroscopic data associated with the cage for compounds synthesized here together with data from related systems previously reported.^{7–9,20,21} The resonances associated with the cage carbons were sensitive to the presence of the metal center. In the case of the monometallic systems, the carbon remote from the ethynyl group was sensitive to the antipodal effect of the electron-donating metal acetylide fragment.²² For example, the acetylide carbon resonances were found at 117.8 (C1) and 82.8 (C10) ppm in **3a**, compared with 104.1 (C1) and 98.3 (C10) in the pro-ligand **1a**. This effect is also evident in the cage C–H ¹H NMR resonances. The ¹¹B NMR spectra are characterized by two (**3a**, **3b**) or one (**4a**, **4b**) resonance, as expected for the symmetry of these molecules. Metalation has a notable effect on the electronic

environment of the ¹¹B nuclei, with these characteristic ¹¹B NMR resonances being found at higher field in the C₂B₈ complexes than in the appropriate trimethylsilyl-protected pro-ligands. It can be concluded that the presence of the metal center, a good electron donor, is reflected in the NMR parameters associated with the atoms of the carborane cage.

X-ray Crystallographic Studies. Single crystals of the new compounds reported here (**1a**, **3a**, **3b**, **4a**, **4b**) were obtained and the compounds structurally characterized (Table 3). The structures of the ethynyl carborane derivatives **1b**,⁹ **2a**¹¹ and **2b**^{9,10,12} have been reported on previous occasions, and selected data are included here for purposes of comparison. Plots of single molecules of **1a**, **3a**, **3b**, **4a** (as the dichloromethane solvate) and **4b** (as a benzene hexasolvate) are shown in Figures 1–5, and selected parameters are summarized in Table 3.

Critical bond parameters associated with the ethynyl carborane **1a** are similar to those found in the closely related diethynyl analogue **2a**; for example, the acetylenic C≡C distances are indistinguishable (Table 3). The C₂B₈ cage in **1a** is distorted from an idealized decahedron, with the cage C–B distances being significantly shorter than the various meridional and

(20) Turner, A. R.; Robertson, H. E.; Borisenko, K. B.; Rankin, D. W. H.; Fox, M. A. *Dalton Trans.* **2005**, 1310.

(21) Fox, M. A.; Greatrex, R.; Greenwood, N. N.; Kirk, M. *Collect. Czech. Chem. Commun.* **1999**, *64*, 806.

(22) Hermanek, S. *Chem. Rev.* **1992**, *92*, 325.

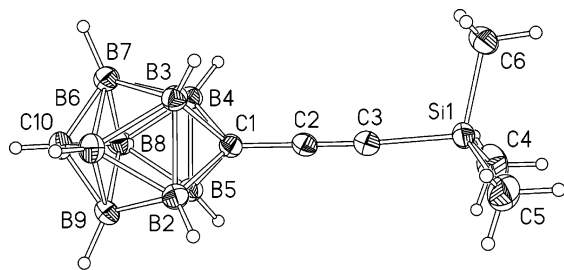


Figure 1. Molecular structure of **1a** showing the atom labeling scheme. In this and all subsequent Figures, displacement ellipsoids shown at the 50% probability level.

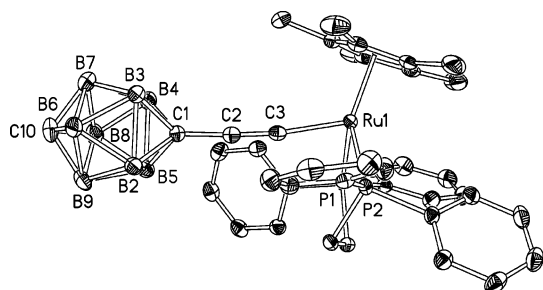


Figure 2. Molecular structure of $[\text{Ru}(1\text{-C}\equiv\text{C}-1,10\text{-C}_2\text{B}_8\text{H}_9)(\text{dppe})\text{Cp}^*]$ (**3a**) showing the atom labeling scheme. Hydrogen atoms are omitted for clarity.

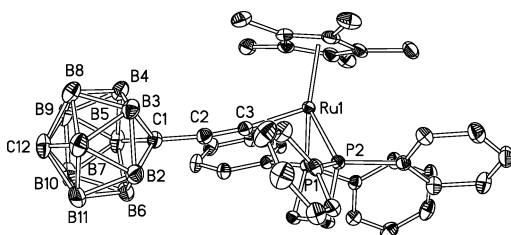


Figure 3. Molecular structure of $[\text{Ru}(1\text{-C}\equiv\text{C}-1,12\text{-C}_2\text{B}_{10}\text{H}_{11})(\text{dppe})\text{Cp}^*]$ (**3b**) showing the atom labeling scheme. Hydrogen atoms are omitted for clarity.

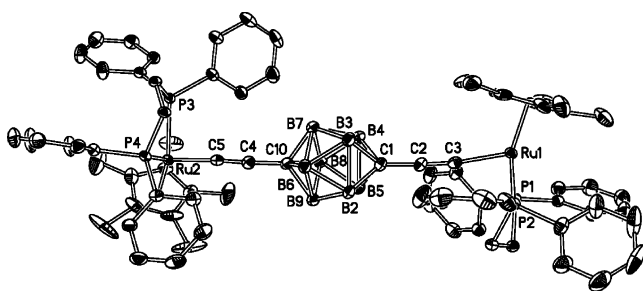


Figure 4. Molecular structure of $[\{\text{Ru}(\text{dppe})\text{Cp}^*\}_2\{\mu\text{-}1,10\text{-}(\text{C}\equiv\text{C})_2\text{-}1,10\text{-C}_2\text{B}_8\text{H}_8\}]$ (**4a**) showing the atom labeling scheme. Hydrogen atoms are omitted for clarity.

tropical B–B distances. Within the extended solid-state structure a C–H $\cdots\pi$ hydrogen-bonding motif is clearly observed (Figure 6).²³

The structures of the mono- and bimetallic ruthenium complexes may be compared with those of the trimethylsilyl-protected pro-ligands and representative metal arylacetylide complexes $[\text{Ru}(\text{C}\equiv\text{CAr})(\text{dppe})\text{Cp}^*]$.¹⁶ The Ru–C(Cp^{*}) distances vary little, falling in the ranges 2.220(2)–2.266(2) Å (**3a**), 2.228(2)–2.265(2) Å (**3b**), 2.213(3)–2.263(3) and 2.215(3)–2.282(3) Å (**4a**) and 2.220(4)–2.258(4) Å (**4b**). Comparisons

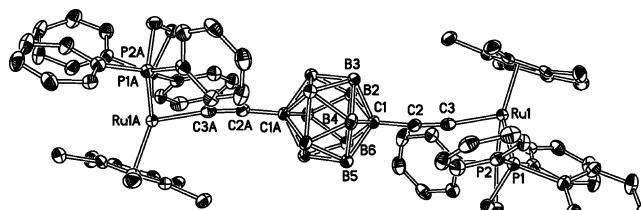


Figure 5. Molecular structure of $[\{\text{Ru}(\text{dppe})\text{Cp}^*\}_2\{\mu\text{-}1,12\text{-}(\text{C}\equiv\text{C})_2\text{-}1,12\text{-C}_2\text{B}_{10}\text{H}_{10}\}]$ (**4b**) showing the atom labeling scheme. Hydrogen atoms are omitted for clarity.

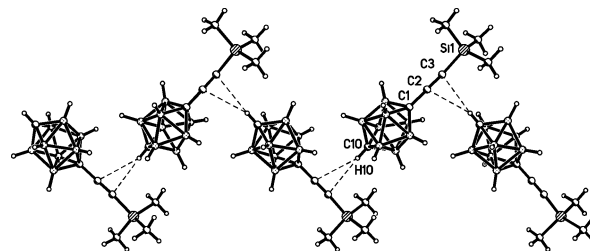


Figure 6. Crystal packing of **1a** illustrating the C–H $\cdots\pi$ (C≡C) hydrogen-bonding motif. Selected distances (Å): C10–H10A, 0.89; H10A \cdots C2, 2.81; H10A \cdots C3, 2.82; C10A \cdots C2, 3.66; C10A \cdots C3, 3.71.

Table 4. Electrochemical Data for Complexes **3a**, **3b**, **4a** and **4b**^a

	E^0 (ox1)	E^0 (ox2)	ΔE^0	K_c
3a	0.35			
3b	0.39			
4a	0.27	0.39	0.12	116
4b	0.32	0.41	0.09	35

^a All E values in V vs SCE. Conditions: 10^{-1} M NBu_4BF_4 in CH_2Cl_2 , glassy carbon working electrode, Pt wire counter and pseudo-reference electrodes, 20 °C, $v = 0.1$ V s^{-1} . The decamethylferrocene/decamethylferrocenium couple ($\text{Fc}^*/\text{Fc}^{*+} = -0.08$ V vs SCE) was used as an internal reference. The observed peak-to-peak separations for each couple are comparable with those from the $\text{Fc}^*/\text{Fc}^{*+}$ internal standard.

of the Ru–P bond lengths reveal average distances of 2.26 Å, with no statistically significant variation as a function of the acetylide substituent. The P–Ru–P angles are similar within the series of complexes reported here, and entirely consistent with values observed for a range of phenyl acetylide complexes reported previously [83.01(2)–84.02(5)°].¹⁶ The Ru–C(1) distances are equivalent within error and marginally shorter than that found in $[\text{Ru}(\text{C}\equiv\text{CC}_6\text{H}_4\text{NH}_2\text{-}4)(\text{dppe})\text{Cp}^*]$ [2.026(3) Å], which could be argued as evidence for the electron-withdrawing nature of the carborane moieties.¹⁶ The distances between the two ruthenium atoms in the bimetallic complexes **4a** and **4b** are 12.6 and 12.4 Å, respectively. This arises from the considerably longer intracage C \cdots C distance in the 10-vertex cage of **4a** than the 12-vertex cage of **4b** in spite of the shorter C(ethynyl)–C(cage) bonds found in **4a** compared to those in **4b** (Table 3).

The C(2)≡C(3) bond lengths are worthy of comment, given the significant discussion of metal–acetylide back-bonding interactions that has often accompanied reports of this parameter.^{16,24,25} On the basis of the data obtained from single-crystal X-ray diffraction, replacement of the trimethylsilyl groups in the trimethylsilylethynyl carborane precursors by the half-sandwich ruthenium centers is found to be accompanied by a

(24) Koentjoro, O. F.; Rousseau, R.; Low, P. J. *Organometallics* **2001**, *20*, 4502.
(25) (a) McGrady, J. E.; Lovell, T.; Stranger, R.; Humphrey, M. G. *Organometallics* **1997**, *16*, 4004. (b) Delfs, C. D.; Stranger, R.; Humphrey, M. G.; McDonoagh, A. M. *J. Organomet. Chem.* **2000**, *607*, 208.

(23) Fox, M. A.; Hughes, A. K. *Coord. Chem. Rev.* **2004**, *248*, 457.

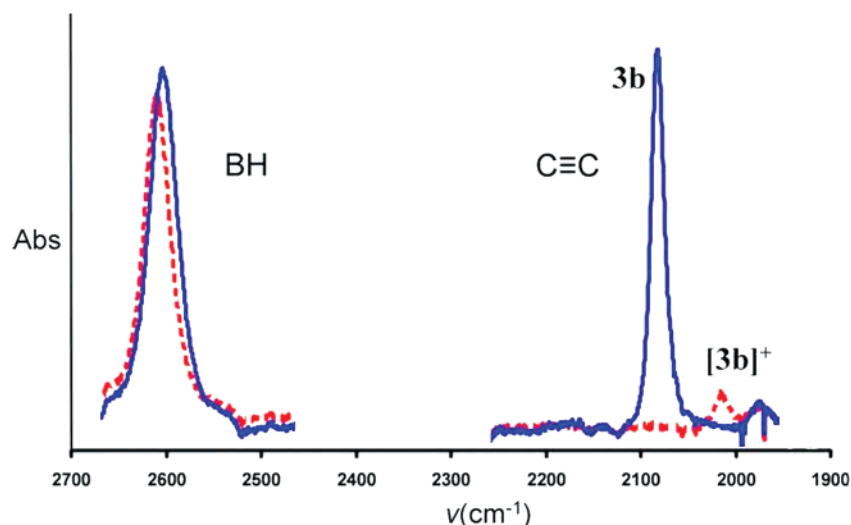


Figure 7. IR spectra obtained in the $\nu(\text{B-H})$ and $\nu(\text{C}\equiv\text{C})$ regions for the monometallic complexes **3b** (solid line [blue]) and **[3b]⁺** (dashed line [red]) in $\text{CH}_2\text{Cl}_2/10^{-1}$ M NBu_4BF_4 at 293 K within an OTTE cell.

small elongation of the acetylide bond length, which is on the borderline of statistical significance (Table 3). Similar structural variations are observed in comparisons made from DFT-optimized geometries of both the carborane precursors and model metal complexes (vide infra).

Electrochemical Studies. The cyclic voltammograms of the mononuclear complexes **3a** and **3b** in $\text{CH}_2\text{Cl}_2/10^{-1}$ M NBu_4BF_4 are each characterized by a single, reversible one-electron anodic wave [$E^\circ = 0.35$ V (**3a**); 0.39 V (**3b**)] (Table 4). These values are close to the oxidation potentials found for $[\text{Ru}(\text{C}\equiv\text{CC}_6\text{H}_4\text{CN})(\text{dppe})\text{Cp}^*]$ (0.36 V) and $[\text{Ru}(\text{C}\equiv\text{CC}_6\text{H}_4\text{NO}_2)(\text{dppe})\text{Cp}^*]$ (0.40 V).¹⁶ Equally, the oxidation of **3a** and **3b** is less thermodynamically favorable than oxidation of $[\text{Ru}(\text{C}\equiv\text{CC}_6\text{H}_5)(\text{dppe})\text{Cp}^*]$ (0.25 V) under the same conditions, providing a qualitative measure of the electron-withdrawing ability of the carborane cage. The bimetallic complexes **4a** and **4b** displayed two sequential reversible waves that were best resolved by square wave voltammetry at 0.27 and 0.39 V (**4a**), and 0.32 and 0.41 V (**4b**). The difference between the potentials gives comproportionation constants $K_c = \exp(\Delta E^\circ F/RT) = 116$ and 35 (at 20°C) associated with **[4a]⁺** and **[4b]⁺**, respectively, which relate to the stability of these compounds with respect to disproportionation under the conditions of the voltammetry measurement, but not necessarily to the “electronic interactions” between the metal centers.²⁶

In an effort to gauge the factors such as ion-pairing in the electrolyte solution that contribute to the stabilization of **[4a]⁺** and **[4b]⁺**, as distinct from inherent electronic factors such as charge delocalization, the voltammetry measurements with **4b** were also carried out using CH_2Cl_2 solutions containing 10^{-1} M $\text{NBu}_4[\text{B}(\text{Ar}_F)_4]$ and NBu_4Cl , as examples of electrolytes with weakly and strongly interacting anions, respectively.²⁷ Differences in the anodic potentials were found to be 70 mV in NBu_4Cl and 80 mV in $\text{NBu}_4[\text{B}(\text{Ar}_F)_4]$. This small decrease in ΔE values indicates that ion pairing is not the only factor contributing to the stability of **[4b]⁺** in solution. To assist in the

characterization of both **[4a]⁺** and **[4b]⁺** we therefore turned to UV–vis–NIR and IR spectroelectrochemical methods, and employed **3a** and **3b** as mononuclear model systems for comparative purposes.

IR Spectroelectrochemical Studies. The complexes **3a**, **3b**, **4a** and **4b** offer $\nu(\text{C}\equiv\text{C})$ and $\nu(\text{B-H})$ bands in the IR region near 2080 and 2600 cm^{-1} , respectively. These characteristic, strong absorptions provide suitable spectroscopic probes through which to study the effect of oxidation on the structure of the ligand using spectroelectrochemical methods. The IR spectra of **3a** and **3b** in $\text{CH}_2\text{Cl}_2/10^{-1}$ M NBu_4BF_4 are similar, with $\nu(\text{C}\equiv\text{C})$ and $\nu(\text{B-H})$ bands at 2083 and 2595 cm^{-1} for **3a**, and 2082 and 2605 cm^{-1} for **3b**. Oxidation to the 17-electron monocations, **[3a]⁺** and **[3b]⁺**, caused the $\nu(\text{C}\equiv\text{C})$ bands to shift to lower frequency (2008 cm^{-1} , **[3a]⁺**; 2014 cm^{-1} , **[3b]⁺**), indicating a significant decrease in the C–C bonding character, with a large drop in intensity (Figure 7). In contrast, the $\nu(\text{B-H})$ band moved to only slightly higher energy (2605 cm^{-1} , **[3a]⁺**; 2614 cm^{-1} , **[3b]⁺**), consistent with only a small reduction in electron density in the carborane cage.

The bimetallic compounds **4a** and **4b** behaved in manner distinct from that of the mononuclear models. Thus, while oxidation to **[4a]⁺**/**[4b]⁺** resulted in a small shift in the $\nu(\text{B-H})$ bands [$\nu(\text{B-H})$: **4a**/**[4a]⁺**, $2592/2602$ cm^{-1} ; **4b**/**[4b]⁺**, $2602/2609$ cm^{-1}], the single $\nu(\text{C}\equiv\text{C})$ bands associated with **4a** (2081 cm^{-1}) and **4b** (2082 cm^{-1}) were replaced by *two* new bands at 2065 , 1990 cm^{-1} (**[4a]⁺**) and 2074 , 2002 cm^{-1} (**[4b]⁺**) (Figure 8). These vibrational bands are superimposed on the low-energy tail of an electronic absorption band (not shown in Figure 8, see below). Subsequent oxidation to **[4a]²⁺** and **[4b]²⁺** was accompanied by a collapse in the electronic absorption band, a further shift of the $\nu(\text{B-H})$ band to higher energy (**[4a]²⁺**, 2607 cm^{-1} ; **[4b]²⁺**, 2617 cm^{-1}), and in each case the $\nu(\text{C}\equiv\text{C})$ region exhibited only one weak $\nu(\text{C}\equiv\text{C})$ band at 2006 (**[4a]²⁺**) or 2012 cm^{-1} (**[4b]²⁺**) (Figure 8). The changes in the IR spectra of **3a**, **3b**, **4a** and **4b** upon the oxidation are consistent with the description of **[4a]⁺** and **[4b]⁺** in terms of a localized mixed-valence model in which the organometallic ethynyl moieties are distinct, at least on the IR time scale (10^{-13} s⁻¹) (Table 5).

(26) (a) Richardson, D. E.; Taube, H. *Coord. Chem. Rev.* **1984**, *60*, 107. (b) Arnold, D. P.; Heath, G. A.; James, D. A. *J. Porphyrins Phthalocyanines* **1999**, *3*, 5. (c) Barrière, F.; Camire, N.; Geiger, W. E.; Mueller-Westerhoff, U. T.; Sanders, R. *J. Am. Chem. Soc.* **2002**, *124*, 7262.

(27) Barrière, F.; Geiger, W. E. *J. Am. Chem. Soc.* **2006**, *128*, 3980.

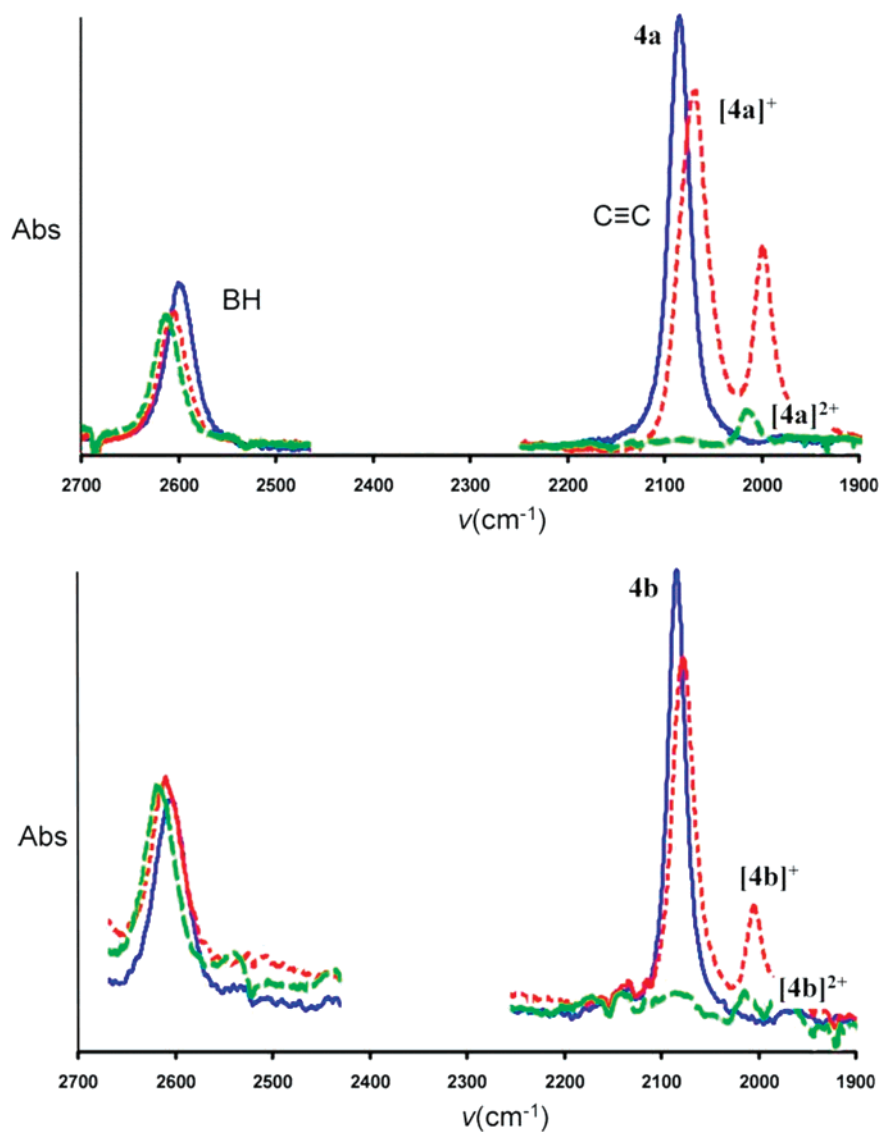


Figure 8. IR spectra obtained in the $\nu(\text{B-H})$ and $\nu(\text{C}\equiv\text{C})$ regions upon oxidation of (a) **4a** and (b) **4b** in $\text{CH}_2\text{Cl}_2/10^{-1}$ M NBu_4BF_4 at 293 K within an OTTLE cell. For clarity, the low-energy tail from the IVCT band has been subtracted (see Figure 11).

Table 5. Observed and Calculated IR Absorptions for Complexes $[\mathbf{3a}]^{n+}$, $[\mathbf{3b}]^{n+}$ ($n = 0, 1$), $[\mathbf{4a}]^{n+}$ and $[\mathbf{4b}]^{n+}$ ($n = 0, 1, 2$)

	obs. $\nu(\text{C}\equiv\text{C})$	calc. ^a $\nu(\text{C}\equiv\text{C})$	Δ^b $\nu(\text{C}\equiv\text{C})$	obs. $\nu(\text{B-H})$	calc. ^a $\nu(\text{B-H})$	Δ^b $\nu(\text{B-H})$
3a	2083	2124	+41	2595	2595	0
[3a]⁺	2008	1983	-25	2605	2605	0
3b	2082	2133	+51	2605	2603	-2
[3b]⁺	2014	1979	-35	2614	2611	-3
4a	2081	2131	+50	2592	2593	+1
[4a]⁺	2065	2055	-10	2602	2605	+3
	1990	1987	-3			
[4a]²⁺	2006	1991(HS)	-15	2607	2610(HS)	+3
		1962(LS)	-44		2616(LS)	+9
4b	2082	2134	+52	2602	2601	-1
[4b]⁺	2074	2091	+17	2609	2611	+2
	2002	1987	-15			
[4b]²⁺	2012	2000(HS)	-12	2617	2616(HS)	-1
		1962(LS)	-50		2616(LS)	-1

^a At MPWIK/3-21G* with frequency correction of 0.92 using the appropriate model system. ^b Difference between observed and computed shifts (calc. - obs.).

UV-vis-NIR Spectroelectrochemical Studies. The electronic spectra of the mononuclear complexes **3a** and **3b** were

characterized by intense transitions in the UV region ($\tilde{\nu} > 35000$ cm^{-1}) that tail into the visible region (Figure 9). A pronounced lower-energy band was also observed for **3a** that proved to be solvatochromic, being observed at 30000 cm^{-1} in acetonitrile and, coincidentally, in 10^{-1} M $\text{NBu}_4\text{BF}_4/\text{CH}_2\text{Cl}_2$ but blue-shifted and obscured by the higher-energy bands in pure CH_2Cl_2 . In general, the electronic absorption spectra of the 17-electron monocations $[\mathbf{3a}]^+$ and $[\mathbf{3b}]^+$ are similar to each other and characterized by bands near 20000 , 15000 , and 7000 cm^{-1} (Figure 9). It is notable, however, that oxidation of **3a** to the 17-electron species $[\mathbf{3a}]^+$ resulted in the collapse of the characteristic absorption band present in **3a** (Figure 9), consistent with the assignment as a metal (or metal ethynyl) to the carborane charge-transfer process. The three absorption features observed in the spectra of $[\mathbf{3a}]^+$ and $[\mathbf{3b}]^+$ below 20000 cm^{-1} are attributable to a $d\pi-(d\pi)^*$ transition and two pseudo-interconfiguration (IC) bands associated with the formally 17-electron, d^5 Ru(III) centers present in these organometallic radical cations. However, given the significant shift in $\nu(\text{C}\equiv\text{C})$ frequencies that accompany oxidation of **3a** and **3b**, the description of transitions in $[\mathbf{3a}]^+$ and $[\mathbf{3b}]^+$ in “metal-centered”

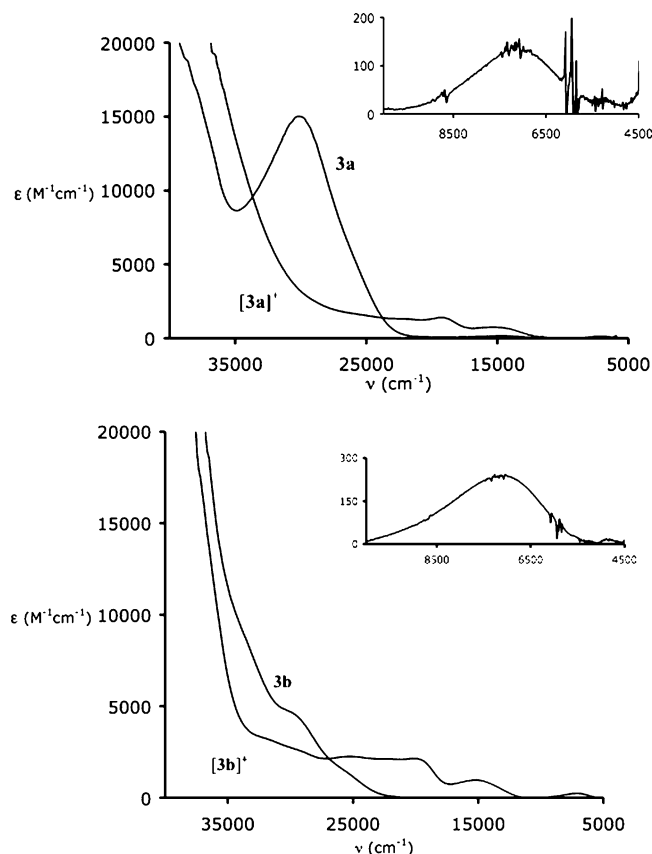


Figure 9. Electronic absorption spectra of **3a** and **[3a]⁺** (upper) and **3b** and **[3b]⁺** (lower) in $\text{CH}_2\text{Cl}_2/10^{-1}$ M NBu_4BF_4 at 293 K, collected within an OTTLE cell. The insets show an expansion of the lower energy region of the monocationic species.

terms is an approximation at best. These electronic spectra are discussed in more detail below; however, the qualitative assignments given here are broadly consistent with the results of time-dependent density functional theory (TD-DFT) calculations.

In a manner that tracks the trends established from the IR spectroscopic work, the electronic spectra of **[4a]ⁿ⁺** and **[4b]ⁿ⁺** ($n = 0, 2$) were similar to the spectra of the mononuclear models **[3a]ⁿ⁺** and **[3b]ⁿ⁺** ($n = 0, 1$). Thus, the electronic spectra of the bimetallic complex **4a** exhibited an unresolved band with a low-energy edge near 25000 cm^{-1} assigned to a $d\pi$ to carborane cage transition (Figure 10). The experimental spectra of the dications **[4a]²⁺** and **[4b]²⁺** were similar to those of the related mononuclear complexes **[3a]⁺** and **[3b]⁺**, with bands near 19000 , 14000 and 7000 cm^{-1} clearly observed, and assigned to $d\pi-(d\pi)^*$ and IC-type transitions. The NIR bands in **[4a]²⁺** and **[4b]²⁺** are well described by a single Gaussian function and are of approximately the same energy, but twice the intensity, of the lowest-energy IC band observed in **[3a]⁺** and **[3b]⁺**. Interestingly, the relatively high-energy $d\pi$ -to-cage transitions associated with the d^6 metal fragments are not observed in the spectra of **[4a]²⁺** and **[4b]²⁺**, and are likely shifted deeper into the UV region, as one would expect on the basis of the lowering of the metal d orbital energies following oxidation.

The compounds **[4a]⁺** and **[4b]⁺** display spectroscopic characteristics of the analogous neutral and dicationic compounds, as well as an additional component within the lowest-energy (NIR) band envelope that extends into the IR region of

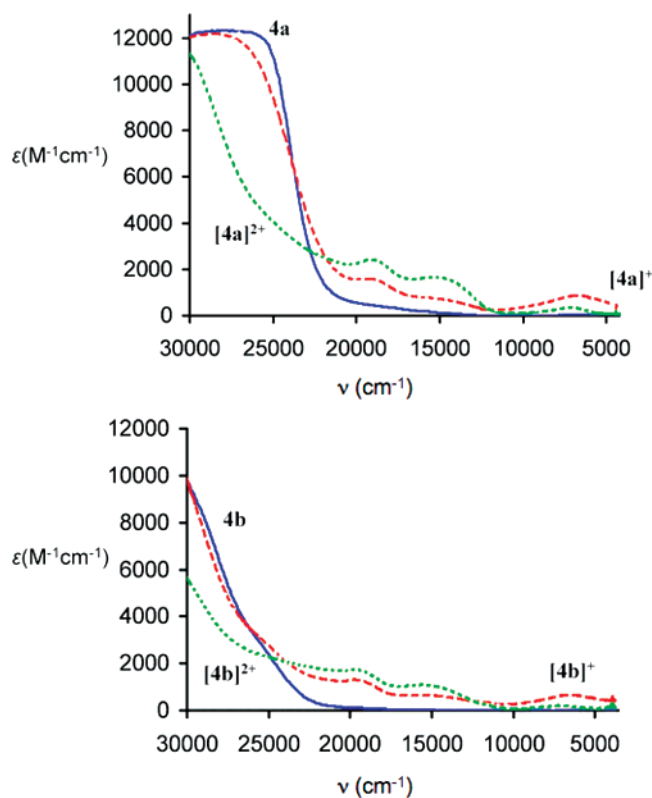


Figure 10. Electronic absorption spectra of **4a**, **[4a]⁺** and **[4a]²⁺** (upper) and **4b**, **[4b]⁺** and **[4b]²⁺** (lower) in $\text{CH}_2\text{Cl}_2/10^{-1}$ M NBu_4BF_4 at 293 K, collected within an OTTLE cell.

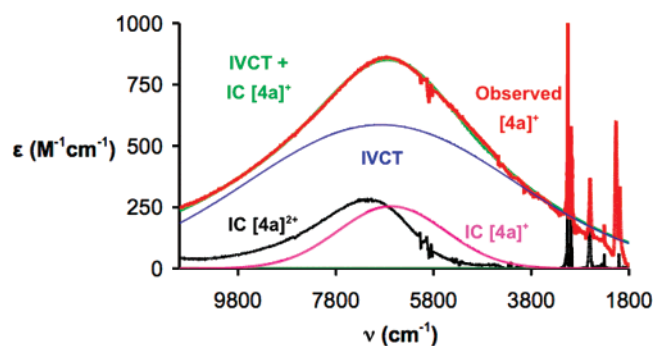


Figure 11. Representative plot showing the low-energy electronic and IR transitions in **[4a]⁺** and **[4a]²⁺**.

the spectrum (Figure 11). These broad absorption bands can be deconvoluted into the sum of two Gaussian components centered at 6870 cm^{-1} ($\epsilon = 590\text{ M}^{-1}\text{ cm}^{-1}$) and 6660 cm^{-1} ($\epsilon = 250\text{ M}^{-1}\text{ cm}^{-1}$) (**[4a]⁺**), and at 5980 cm^{-1} ($\epsilon = 350\text{ M}^{-1}\text{ cm}^{-1}$) and 6640 cm^{-1} ($\epsilon = 200\text{ M}^{-1}\text{ cm}^{-1}$) (**[4b]⁺**). On the basis of the assignments made from the mononuclear analogue, they may be regarded as representing the intervalence charge transfer (IVCT) transition and a localized Ru(III) IC transition, respectively.

The more intense, presumably IVCT components of the NIR bands in **[4a]⁺** ($\bar{\nu}_{\text{max}} = 6870\text{ cm}^{-1}$) and **[4b]⁺** ($\bar{\nu}_{\text{max}} = 5980\text{ cm}^{-1}$) offer half-height band widths, $\Delta\bar{\nu}_{1/2}$, (**[4a]⁺** 6400 cm^{-1} , **[4b]⁺** 5040 cm^{-1}) considerably larger than that predicted from the Hush relationship $\Delta\bar{\nu}_{1/2} = (2310 \bar{\nu}_{\text{max}})^{1/2}$ (**[4a]⁺** $\approx 4000\text{ cm}^{-1}$, **[4b]⁺** $\approx 3410\text{ cm}^{-1}$), consistent with class II behavior. From these data, and taking the Ru \cdots Ru distance obtained from the optimized geometries as an approximation of the electron-transfer distance (**[4a]⁺** 12.56 \AA , **[4b]⁺** 12.32 \AA), coupling

Table 6. Comparison of Selected Bond Lengths (Å) and Dihedral Angle (deg) of X-ray Structures of **3a** and **3b** and from the MPW1K/3-21G* Optimized Structures of **[3a-H]ⁿ⁺** and **[3b-H]ⁿ⁺** ($n = 0, 1$)

	3a	3a-H	[3a-H]⁺	3b	3b-H	[3b-H]⁺
Ru–C(3)	1.999(2)	1.998	1.940	2.003(2)	1.997	1.937
C(3)–C(2)	1.214(3)	1.217	1.230	1.214(2)	1.216	1.233
C(2)–C(1)	1.443(3)	1.409	1.404	1.439(2)	1.419	1.419
C(1)–B ^a	1.619(3)	1.629	1.625	1.726(4)	1.734	1.737
B–B ^b	1.845(4)/1.808(4)	1.863/1.809	1.875/1.804	1.778(9)/1.760(6)	1.791/1.767	1.808/1.769
C(10/12)–B ^a	1.595(4)	1.613	1.613	1.700(6)	1.714	1.720
Ru–P	2.267(1)	2.254	2.300	2.259(1)	2.255	2.305

^a Averaged values. ^b The two values represent the two distinct B–B bonds in the *p*-carborane geometries; see Table 3.

Table 7. Comparison of Selected Bond Lengths (Å) and Dihedral Angle (deg) of X-ray Structures of **4a** and **4b** and from the MPW1K/3-21G* Optimized Structures of **[4a-H]ⁿ⁺** and **[4b-H]ⁿ⁺** ($n = 0, 1, 2$)

	4a	4a-H	[4a-H]⁺	[4a-H]²⁺ (LS)	[4a-H]²⁺ (HS)
Ru–C(3)	2.000(3)	1.999	1.976/1.931	1.920	1.947
C(3)–C(2)	1.214(4)	1.217	1.223/1.232	1.241	1.227
C(2)–C(1)	1.431(4)	1.409	1.396	1.379	1.407
C(1)–B ^a	1.622(5)	1.628	1.630	1.640	1.627
B–B ^b	1.845(5)/1.802(5)	1.861/1.805	1.871/1.802	1.881/1.800	1.873/1.805
Ru–P	2.268(2)	2.254	2.261/2.294	2.285	2.313
θ^c	133.5	179.9	167.6	179.2	158.6
	4b	4b-H	[4b-H]⁺	[4b-H]²⁺ (LS)	[4b-H]²⁺ (HS)
Ru–C(3)	1.991(4)	1.998	1.984/1.932	1.926	1.950
C(3)–C(2)	1.205(4)	1.216	1.220/1.230	1.238	1.225
C(2)–C(1)	1.454(5)	1.420	1.412	1.399	1.420
C(1)–B ^a	1.726(6)	1.733	1.730	1.738	1.731
B–B ^b	1.774(6)/1.756(6)	1.790/1.766	1.795/1.766	1.801/1.764	1.803/1.765
Ru–P	2.257(2)	2.254	2.260/2.300	2.285	2.314
θ^c	180.0	179.9	163.6	180.0	160.4

^a Averaged values. ^b The two values represent the two distinct B–B bonds in the *p*-carborane geometries, see Table 3. ^c The angle θ is defined as the dihedral angle C(0)–Ru···Ru–C(0), where C(0) represents the centroid of the Cp ring.

parameters H_{ab} of 260 cm⁻¹ (**[4a]⁺**) and 140 cm⁻¹ (**[4b]⁺**) can be estimated.¹

DFT-Optimized Geometries and Vibrational Spectroscopy. DFT calculations (MPW1K/3-21G*) have been performed without symmetry constraints, using models that employ Ru-(PH₃)₂Cp fragments rather than the Ru(dppe)Cp* moiety to reduce computational effort, and are denoted **[3a-H]ⁿ⁺**, **[3b-H]ⁿ⁺**, **[4a-H]ⁿ⁺** and **[4b-H]ⁿ⁺**. The critical geometric features of **3a-H**, **3b-H**, **4a-H** and **4b-H** are similar and are also broadly in keeping with geometries of other half-sandwich ruthenium acetylides such as [Ru(C≡CR)(PH₃)₂Cp] (R = H, Ph)^{15d,24,25,29} and the crystallographically determined structures of **3a**, **3b**, **4a** and **4b** (Tables 6 and 7). Comparisons between the structures of **3a-H** and **[3a-H]⁺**, and also between **3b-H** and **[3b-H]⁺**, reveal variations in keeping with previous studies on related systems.²⁹ Thus, there is an elongation of the C(3)≡C(2) and Ru–P bonds and a complementary contraction of the Ru–C(3) bond as a consequence of the loss of a single electron from the neutral compounds. Interestingly, the geometric parameters associated with the carborane cages in each pair of compounds **[3a-H]ⁿ⁺** and **[3b-H]ⁿ⁺** ($n = 0, 1$) are largely unchanged, although some small expansion of the cage is evidenced (Table 6).

DFT-based calculations using B3LYP and related functionals can fail to adequately model “valence-trapped” (i.e., class II) mixed-valence systems, with geometry optimization affording

Table 8. Energy (ε/eV), Occupancy (occ) and Composition (%) of Selected Frontier Orbitals for **3a-H** and **3b-H**

	HOMO–2	HOMO–1	HOMO	LUMO	LUMO+1	LUMO+2	LUMO+3
3a-H							
ε	–7.14	–6.70	–6.42	–0.35	–0.35	0.21	0.56
occ	2	2	2	0	0	0	0
Cp	29	7	11	0	0	24	1
PH ₃	11	4	5	1	1	27	12
Ru	31	51	40	2	2	49	86
C(3)	12	10	10	4	4	0	1
C(2)	12	22	27	0	0	0	0
C ₂ B ₈	4	6	7	93	92	0	1
3b-H							
ε	–7.22	–6.78	–6.51	0.17	0.52	0.64	0.67
occ	2	2	2	0	0	0	0
Cp	27	10	12	23	1	1	1
PH ₃	10	5	6	28	10	2	4
Ru	30	54	41	49	79	7	12
C(3)	13	8	9	0	1	7	7
C(2)	10	19	27	0	0	2	1
C ₂ B ₁₀	4	4	6	0	10	81	76

structures in which the two metal moieties are in the same geometric and electronic environment.³⁰ In the present case, the MPW1K calculations, with a significant HF component,³¹ optimize an asymmetric geometry for both **[4a-H]⁺** and **[4b-H]⁺** that resembles the “valence-trapped” model. Thus, one of the metal–ethynyl moieties in each cation **[4a-H]⁺** and **[4b-H]⁺** displays elongated C(3)≡C(2) and Ru–P bonds and a contracted Ru–C(3) bond and closely resembles the optimized geometry of the related mononuclear systems **[3a-H]⁺** or **[3b-**

(28) (a) Hush, N. S. *Prog. Inorg. Chem.* **1967**, *8*, 391. (b) Hush, N. S. *Trans. Faraday Soc.* **1961**, *57*, 557. (c) Hush, N. S. *Electrochim. Acta* **1968**, *13*, 1005.

(29) Fox, M. A.; Roberts, R. L.; Khairul, W. M.; Hartl, F.; Low, P. J. *J. Organomet. Chem.* **2007**, *692*, 3277.

(30) Maurer, J.; Sarkar, B.; Schwederski, B.; Kaim, W.; Winter, R. F.; Zális, S. *Organometallics* **2006**, *25*, 3701.

(31) (a) Lynch, B. J.; Fast, P. L.; Harris, M.; Truhlar, D. G. *J. Phys. Chem. A* **2000**, *104*, 4811. (b) Lynch, B. J.; Zhao, Y.; Truhlar, D. G. *J. Phys. Chem. A* **2003**, *107*, 1384.

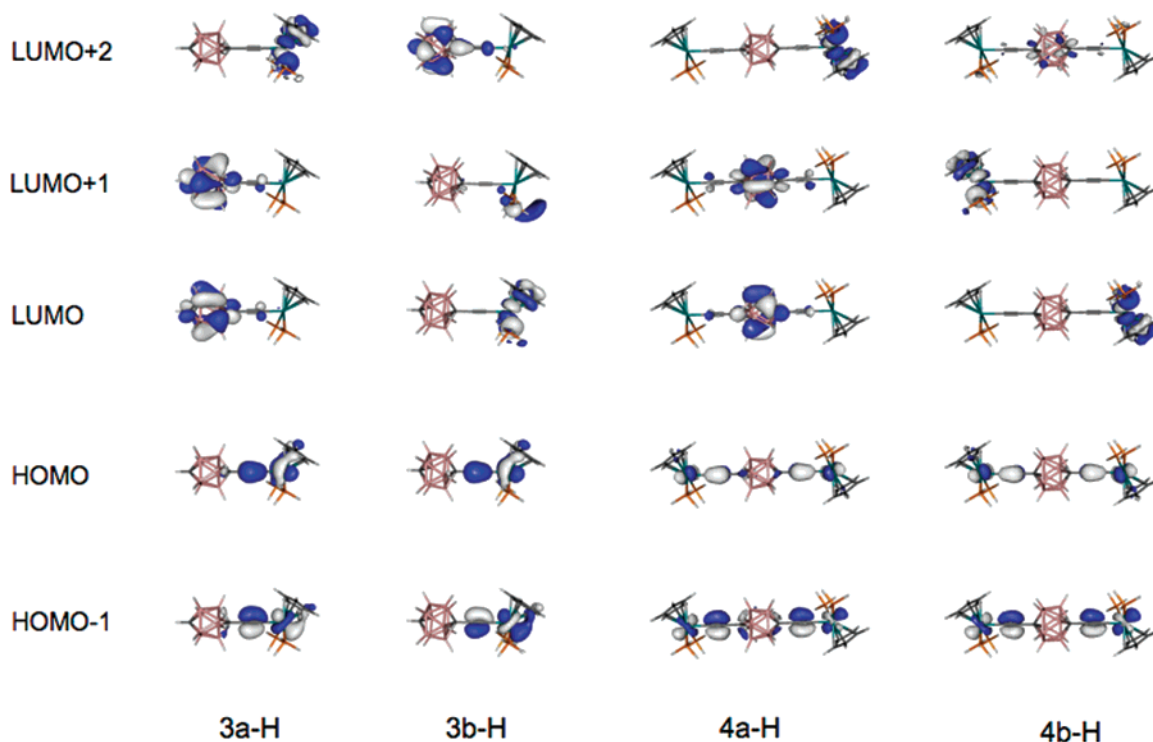


Figure 12. Frontier orbitals of **3a-H**, **3b-H**, **4a-H** and **4b-H**. Contour values are plotted at ± 0.04 (e/bohr^3)^{1/2}.

H]⁺. The other is more or less unchanged from the precursor **4a-H** or **4b-H** and the mononuclear model **3a-H** or **3b-H** as appropriate (Table 7). Vibrational frequency calculations based on these asymmetric geometries are in excellent agreement with the IR spectroelectrochemical results (Table 5). Two $\nu(\text{C}\equiv\text{C})$ bands are calculated, falling within 20 cm^{-1} of the observed bands. The $\nu(\text{B}-\text{H})$ band is largely unaffected by the number of electrons in the model system and is calculated at ~ 2600 cm^{-1} in agreement with the experimental observations.

The dications [**4a-H**]²⁺ and [**4b-H**]²⁺ offer two potential spin states, namely a singlet, low-spin (LS) configuration and a triplet, high-spin (HS) configuration. In contrast to the polyynediyl-bridged analogues $\{[\text{Ru}(\text{PR}_3)_2\text{Cp}]_2\{\mu-(\text{C}\equiv\text{C})_n\}\}^{2+}$,^{15c,d} the triplet (high spin, HS) configurations of [**4a-H**]²⁺ and [**4b-H**]²⁺ are computed to be more stable ([**4a-H**]²⁺, 34 kcal mol^{-1} ; [**4b-H**]²⁺, 37 kcal mol^{-1}) than the singlet (low-spin, LS) states. While the calculated IR spectra of the HS and LS states are similar, the HS model ($\theta = 160^\circ$) provides the best agreement with the experimental data (Table 5). Within the geometry-optimized (HS) models [**4a-H**]²⁺ and [**4b-H**]²⁺ the environments at both metal centers are indistinguishable, and similar to those of the mononuclear systems [**3a**]⁺ and [**3b-H**]⁺, respectively. The preference for the HS diradical species is perhaps an indication that the carboranes act more effectively as physical spacers than as strong electronic coupling elements in the dications. Given the lower energy of the HS systems and the better match between the calculated and observed IR data, we will only refer to the triplet states in the following discussions.

Electronic Structures and TD-DFT Studies. An analysis of the energies and composition of the MOs derived from **3a-H**, **3b-H**, **4a-H** and **4b-H** reveals the same general electronic structure as has been found in previous studies of $[\text{Ru}(\text{C}\equiv\text{CAryl})(\text{PR}_3)_2\text{Cp}']$ -based systems.^{16,24,25,29} In all cases the two highest-lying occupied MOs are largely centered on the Ru–

Table 9. Energy (ϵ/eV), Occupancy (occ) and Composition (%) of Selected Frontier Orbitals for **4a-H** and **4b-H**

	HOMO–2	HOMO–1	HOMO	LUMO	LUMO+1	LUMO+2	LUMO+3
4a-H							
ϵ	–6.43	–6.33	–6.04	–0.17	–0.17	0.35	0.37
occ	2	2	2	0	0	0	0
Cp(1)	7	1	4	0	0	23	0
PH ₃ (1)	3	1	2	1	1	28	0
Ru(1)	22	19	17	2	2	49	0
C3(1)	4	9	7	4	4	0	0
C2(1)	13	13	14	0	0	0	0
C ₂ B ₈	5	11	9	86	86	0	0
C2(2)	12	14	15	0	0	0	0
C3(2)	3	9	7	4	4	0	0
Ru(2)	21	21	18	2	2	0	49
PH ₃ (2)	3	1	2	1	0	0	28
Cp(2)	6	2	5	0	0	0	23
4b-H							
ϵ	–6.49	–6.48	–6.18	0.33	0.33	0.64	0.69
occ	2	2	2	0	0	0	0
Cp(1)	7	2	5	23	1	0	0
PH ₃ (1)	3	1	2	27	1	3	6
Ru(1)	23	24	19	48	1	30	44
C3(1)	3	7	6	0	0	2	0
C2(1)	12	13	14	0	0	1	0
C ₂ B ₁₀	4	7	7	0	0	28	0
C2(2)	12	13	14	0	0	1	0
C3(2)	3	7	6	0	0	2	0
Ru(2)	22	24	19	1	48	30	44
PH ₃ (2)	3	1	2	1	27	3	6
Cp(2)	7	3	5	1	23	0	0

ethynyl groups of the molecules, being π -type in character, nearly orthogonal to each other, antibonding with respect to Ru–C(3), and bonding with respect to C(3)–C(2) (Table 8, Table 9, Figure 12).

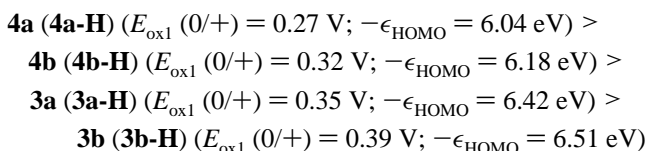
There are negligible contributions from the cage to the HOMOs. In general, the lowest-lying unoccupied orbitals of $[\text{Ru}(\text{C}\equiv\text{CAryl})(\text{PH}_3)_2\text{Cp}]$ systems are metal and metal–Cp in character, although the introduction of strongly electron-withdrawing groups can lower an acetylide ligand-based orbital

Table 10. Comparison of Electronic Transitions on Model Geometries [3a-H]ⁿ⁺, [3b-H]ⁿ⁺ (n = 0, 1), [4a-H] and [4b-H]ⁿ⁺ (n = 0, 1, 2) based on TD-DFT Calculations (MPW1K/3-21G*) with Experimental UV-Vis-NIR Data for Complexes [3a]ⁿ⁺, [3b]ⁿ⁺ (n = 0, 1), [4a]ⁿ⁺ and [4b]ⁿ⁺ (n = 0, 1, 2)

model	main components of transition	transition type ^a	energy (eV, cm ⁻¹)	oscillation strength	compound	transition (cm ⁻¹)	ϵ (M ⁻¹ cm ⁻¹)
3a-H	HOMO→LUMO, HOMO→(LUMO+1)	RuCC → cage	4.50 (36360)	0.0437	3a	30395	15000
[3a-H]⁺	(β-HOSO-1)→β-LUSO	CpRu → RuCC	1.17 (9450)	0.0005	[3a]⁺	7485	125
	(β-HOSO-2)→β-LUSO	CpRuCC → RuCC	2.47 (19960)	0.1966		15300	750
	(β-HOSO-5)→β-LUSO	CpRu → RuCC	3.13 (25250)	0.0012		19650	1400
	α-HOSO→α-LUSO	RuCC → RuCp	3.44 (27850)	0.0164		22520	1330
3b-H	HOMO→(LUMO+2), HOMO→(LUMO+3)	RuCC → cage	5.41 (43670)	0.0372	3b	<30000	-
[3b-H]⁺	(β-HOSO-1)→β-LUSO	CpRu → RuCC	1.13 (9160)	0.0006	[3b]⁺	7300	240
	(β-HOSO-2)→β-LUSO	CpRuCC → RuCC	2.49 (20080)	0.1693		15290	965
	(β-HOSO-7)→β-LUSO	CpRu → RuCC	2.82 (22830)	0.0094		20160	2100
	α-HOSO→α-LUSO	RuCC → RuCp	3.40 (27550)	0.0149		25500	2250
4a-H	HOMO→LUMO, HOMO→(LUMO+1)	RuCC → cage	4.29 (34700)	0.0942	4a	26180	12200
[4a-H]⁺	(β-HOSO-4)→β-LUSO	CpRu → RuCC (IC)	0.43 (3520)	0.0671	[4a]⁺	6660	250
	β-HOSO→β-LUSO	RuCC → RuCC (IVCT)	0.53 (4300)	0.3056		6870	590
	(β-HOSO-3)→β-LUSO	RuCC → RuCC	2.31 (18650)	0.0779		15575	730
	(β-HOSO-9)→β-LUSO	CpRuCC → RuCC	2.60 (21000)	0.0460		19350	1590
[4a-H]²⁺	(β-HOSO-2)→β-LUSO	CpRu → RuCC	1.06 (8550)	0.0012	[4a]²⁺	7300	340
	(β-HOSO-4)→β-LUSO	CpRuCC → RuCC	2.50 (20200)	0.4643		15240	1660
	(β-HOSO-6)→β-LUSO	CpRu → RuCC	2.81 (22700)	0.0110		19265	2400
4b-H	HOMO→(LUMO+4), HOMO→(LUMO+5)	RuCC → cage	5.23 (42370)	0.1090	4b	<30000	-
[4b-H]⁺	(β-HOSO-6)→β-LUSO	RuCC → RuCC (IC)	0.48 (3910)	0.0226	[4b]⁺	6640	200
	β-HOSO→β-LUSO	RuCC → RuCC (IVCT)	0.59 (4740)	0.1950		5980	350
	(β-HOSO-3)→β-LUSO	CpRu → RuCC	2.37 (19160)	0.0872		14620	620
	(β-HOSO-9)→β-LUSO	CpRuCC → RuCC	2.58 (20870)	0.0636		19680	1300
[4b-H]²⁺	(β-HOSO-3)→(β-LUSO+1), (β-HOSO-2)→β-LUSO	CpRu → RuCC	1.03 (8360)	0.0011	[4b]²⁺	7220	200
	(β-HOSO-5)→(β-LUSO+1), (β-HOSO-4)→β-LUSO	CpRuCC → RuCC	2.57 (20790)	0.3931		15360	1070
	(β-HOSO-7)→(β-LUSO+1), (β-HOSO-6)→β-LUSO	CpRu → RuCC	2.81 (22675)	0.0221		19645	1740

^a IC = interconfigurational transition, IVCT = inter-valence charge-transfer transition.

into this region.^{16,29,32} In the context of the present examples, the complexes **3a-H** and **4a-H**, which feature the smaller carborane cage, also offer low-lying, largely cage-centered unoccupied orbitals, which are similar in energy to the metal-based LUMOs. The energy of the various frontier MOs of **3a-H**, **3b-H**, **4a-H** and **4b-H** together with the orbital composition are summarized in Tables 8 and 9, and represented graphically in Figure 12. Although Koopmans' theorem ignores electron correlation and similar effects, it is interesting to note that the solution-phase oxidation potentials obtained from the cyclic voltammetry data (Table 4) track the calculated HOMO energies and show the similar trends, i.e., the ease of the first oxidation being



Electronic spectroscopy coupled with TD-DFT calculations provides a convenient method through which to link the results of electronic structure calculations with experiment. Detailed TD-DFT results are included in the Supporting Information, and important results are summarized in Table 10, to both aid in the assignment of the electronic spectra and support the results of the electronic structure calculations. The lowest-energy absorption bands of any appreciable intensity in the mononuclear model **3a-H**, calculated to fall near 36000 cm⁻¹, corresponds to a (dπ)* → cage charge-transfer band, which correlates with

Table 11. Calculated Spin Densities (MPW1K/3-21G*) for Cations [3a-H]⁺, [3b-H]⁺, [4a-H]⁺ and [4b-H]⁺ and Triplet States of [4a-H]²⁺ and [4b-H]²⁺

	Ru(1)	C3(1)	C2(1)	C1(1)	Ru(2)	C3(2)	C2(2)	C1(2)
[3a-H]⁺	0.683	-0.187	0.457	-0.050				0.012
[3b-H]⁺	0.647	-0.155	0.445	-0.042				0.006
[4a-H]⁺	0.517	-0.097	0.390	-0.033	0.060	0.033	0.037	0.018
[4b-H]⁺	0.607	-0.152	0.435	-0.041	0.029	0.017	0.018	0.008
(HS)-[4a-H] ²⁺	0.734	-0.211	0.428	-0.041				
(HS)-[4b-H] ²⁺	0.749	-0.221	0.428	-0.041				

the solvatochromic behavior of the experimentally observed band at 30000 cm⁻¹ in **3a**. The analogous transitions in **3b-H** are calculated at significantly higher energy, near 45000 cm⁻¹, accounting for the blue shift of this band in **3b**. In the case of the models [3a-H]⁺ and [3b-H]⁺ the highest occupied α-spin orbitals (α-HOSO) and lowest unoccupied β-spin orbitals (β-LUSO) offer considerable metal and ethynyl character and have similar nodal properties and atomic composition as the HOMOs in the 18-electron precursors. The calculated spin densities are summarized in Table 11. The ruthenium center and the C(2) carbon carry the largest positive spin density, the proportions of which are largely insensitive to the nature of the cage. These electronic structure calculations are in agreement with the spectroelectrochemical results and indicate that the oxidation of the mononuclear complexes is largely associated with the removal of an electron from a metal-ethynyl-based MO.

TD-DFT calculations involving the oxidized model species [3a-H]⁺ or [3b-H]⁺ give good agreement with the experimentally observed absorption bands. These bands may be approximately described as the dπ-(dπ)* and IC transitions associated with the formally d⁵ Ru(III) center, although the mixing of the metal orbitals with the ethynyl and other

(32) Powell, C. E.; Cifuentes, M. P.; McDonagh, A. M.; Hurst, S. K.; Lucas, N. T.; Delfs, C. D.; Stranger, R.; Humphrey, M. G.; Houbrechts, S.; Asselberghs, I.; Persoons, A.; Hockless, D. C. R. *Inorg. Chim. Acta* **2003**, *352*, 9.

supporting ligands should be noted (Table 10). The α -HOSO \rightarrow α -LUSO transition is also apparent.

For each bimetallic carborane-bridged complex **4a-H** and **4b-H**, the HOMO is composed of contributions from the pseudo-linear Ru–C \equiv C–cage–C \equiv C–Ru assembly, with significant Ru d and C \equiv C π character, and is removed in energy from the other frontier orbitals. In the case of **4a-H** the lowest unoccupied orbitals are degenerate and localized on the carborane cage, with an almost degenerate pair of unoccupied metal-based orbitals somewhat higher in energy. The lowest energy unoccupied orbitals of **4b-H** are more Cp-metallic in character (Table 10, Figure 12).

The electronic spectrum of **4a** exhibited an unresolved band with a low-energy edge near 25000 cm⁻¹, while only the tail of this band was apparent in the spectrum of **4b**. The TD-DFT calculations on the model **4a-H** indicate this band is likely due to excitations between the largely metal–ethynyl-localized HOMO (Figure 12) to the cage-based LUMOs. Electronic structure calculations performed on the larger-cage model **4b-H** suggest that the analogous transitions between metal–ethynyl HOMOs and the unoccupied orbitals on the C₂B₁₀ cage are significantly higher in energy. In addition to this approximately metal–ethynyl to cage charge-transfer band, the intermediate oxidation states ([**4a**]⁺ or [**4b**]⁺) also feature bands in the visible region near 20000 and 15000 cm⁻¹, and a relatively broad absorption band in the NIR region (Figure 11). These new bands are similar in energy and intensity to the $d\pi$ –($d\pi$)^{*} and IC transitions observed for the mononuclear complexes and can be identified as such from the TD-DFT calculations, although the transitions do involve a considerable degree of mixing of character from both metal moieties (Table 10).

Perhaps of most interest are the transitions that comprise the NIR band envelopes in the mixed-valence cations [**4a**]⁺ and [**4b**]⁺. These bands are considerably broader and more intense than the IC transitions associated with [**3a**]⁺ and [**3b**]⁺ and, as indicated above, can be deconvoluted into a sum of two Gaussian curves, which are associated with the IC style transitions localized on the formally d⁵ Ru(III) component of the mixed-valence compound, and the other, more intense and broader component which is the true IVCT portion of the band envelope (Table 10). These assignments are also supported by the TD-DFT calculations, which predict a lower-intensity component with a “dd” character from the “d⁵” site, albeit admixed with similar orbitals on the “d⁶” metal fragment, together with a transition largely composed of the β -HOSO and β -LUSO orbitals (Figure 13) and which corresponds to the IVCT transition.

The experimental spectra of the dications [**4a**]²⁺ and [**4b**]²⁺ were similar to those of the related mononuclear complexes [**3a**]⁺ and [**3b**]⁺, with bands near 19000, 14000 and 7000 cm⁻¹ clearly observed, and also reproduced in the computational models (Table 10). Interestingly, the relatively high-energy $d\pi$ -to-cage transitions associated with the complexes featuring formally d⁶ metal fragments are not observed in the spectra of [**4a**]²⁺ and [**4b**]²⁺, and according to the TD-DFT results should be shifted deeper into the UV region, as one would expect on the basis of the lowering of the metal d orbital energies following oxidation.

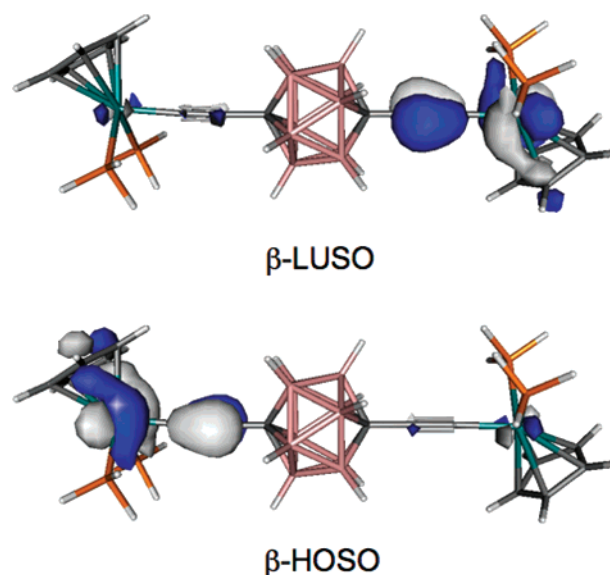


Figure 13. β -LUSO and β -HOSO of [**4b**]⁺. Contour values are plotted at ± 0.04 (e/bohr³)^{1/2}.

Conclusions

Trimethylsilyl-protected ethynyl 10- and 12-vertex *p*-carboranes are convenient reagents for use in the preparation of mono- and bimetallic acetylide complexes containing *p*-carborane cages. These four ruthenium complexes undergo one or two sequential oxidation events at moderate potentials, which can be observed voltammetrically, and the resulting oxidation products are characterized by UV–vis–NIR and IR spectroelectrochemical methods. A combination of spectroscopic data and computational studies reveals that the carborane orbitals do not mix significantly with the metal–ethynyl-based orbitals. The stabilization of the mixed-valence states arises not entirely from ion pairing with the electrolyte but also from an inherent electronic effect. Both 10- and 12-vertex cages appear to permit electronic communication between the two metal centers over a distance of ca. 12.5 Å with the 10-vertex cage leading to a slightly higher coupling parameter, based on treatment of the data according to the Hush model. The LUMOs in the 10-vertex cage complexes have cage character and metal-to-cage transfer bands were observed in the UV spectra of these compounds. The carborane cages, particularly the better-known 12-vertex analogue, are perhaps best described as *pseudo*-aromatic spherical spacers, that in the cases described here permit a degree of interaction between two metal centers. Geometries of the “valence-localized” mixed-valence compounds [**4a**]⁺ and [**4b**]⁺, and the other compounds reported here, were satisfactorily modeled using the MPW1K/3-21G* level of theory, and the spectroscopic transitions observed, including the “IVCT” band, were successfully modelled with TD-DFT methods.

Terminology such as “intervalence charge transfer” was developed from studies of classical mixed-valence coordination complexes and presupposes metal-centered redox processes and assignment of well-defined metal d-electron counts. In many organometallic complexes the mixing of metal, supporting and bridging ligand orbitals arguably makes such terms less appropriate. With the optimization of suitable geometries that satisfactorily model the “valence-localized” case, TD-DFT methods may be used to provide an alternative, molecular

orbital-based description of the fascinating spectroscopic properties of “valence-localized mixed-valence” organometallic compounds.

Experimental Section

All reactions were carried out under an atmosphere of dry nitrogen, using standard Schlenk techniques. Reaction solvents were purified and dried using an Innovative Technology SPS-400, and degassed before use. No special precautions were taken to exclude air or moisture during workup. The compounds [RuCl(dppe)Cp*],³³ **1a**, **1b**,⁹ **2a**⁷ and **2b**⁷ were prepared by the literature methods or minor variations as described in the Supporting Information. Other reagents were purchased and used as received.

Cyclic voltammograms were recorded from solutions of approximately 10⁻⁴ M in analyte in dichloromethane containing 10⁻¹ M NBu₄-BF₄ (recrystallized twice from absolute ethanol and dried overnight under vacuum at 80 °C before use) at $\nu = 100 \text{ mV s}^{-1}$ in a gas-tight single-compartment three-electrode cell equipped with glassy carbon disk working (apparent surface area of 0.42 mm²), coiled platinum wire auxiliary, and platinum wire pseudo-reference electrodes. All redox potentials are reported against the SCE scale, with the decamethylferrocene/decamethylferrocenium (Fc^{*}/Fc⁺) redox couple used as an internal reference system: -0.08 V vs SCE.³⁴ Data were collected using a computer-interfaced EcoChemie PGSTAT-30 potentiostat.

Spectroelectrochemical experiments at room temperature were performed with an airtight optically transparent thin-layer electrochemical (OTTLE) cell equipped with a Pt minigrad working electrode (32 wires cm⁻¹) and CaF₂ windows.³⁵ The cell was positioned in the sample compartment of a Nicolet Avatar FT-IR spectrometer (1 cm⁻¹ spectral resolution, 16 scans) or a Perkin-Elmer Lambda-900 spectrophotometer. The controlled-potential electrolyses were carried out with a potentiostat constructed in-house.

General Procedure: Preparation of [Ru(1-C≡C-1,10-C₂B₈H₉)-(dppe)Cp*] (3a). A suspended mixture of [RuCl(dppe)Cp*] (100 mg, 0.15 mmol), **1a** (35 mg, 0.165 mmol), and KF (15 mg, 0.25 mmol) in methanol (20 mL) was refluxed for 6 h. The yellow precipitate formed was filtered and washed with ice-cold methanol to give **3a** as a yellow solid (75 mg, 69%). Recrystallization of the solid from dichloromethane/methanol gave yellow crystals suitable for X-ray crystallography. IR (KBr disc, cm⁻¹): 3100w cage CH, 3076, 3054w phenyl CH, 2962w, 2908w, 2856w aliphatic CH, 2591s BH, 2074s C≡C, 1433 m, 1095 m, 697s, 533s. ¹H{¹¹B} NMR (CDCl₃): δ 1.58 (s, 15H, Me), 1.66 (s, 4H, B2-5H), 1.83 (s, 4H, B6-9H), 2.12 (m, 2H, CH₂), 2.75 (m, 2H, CH₂), 6.01 (s, 1H, C10H), 7.30 (m, 16H, Ph), 7.81 (m, 4H, Ph). ³¹P{¹H} NMR (CDCl₃): δ 81.6 (s). ¹¹B NMR (CDCl₃): δ -11.3 (d, 4B, J_{BH} = 164 Hz, B2-5), -15.7 (d, 4B, J_{BH} = 162 Hz, B6-9). ¹³C{¹H} NMR: δ 10.0 (Me), 29.5 (m, CH₂), 82.8 (C10), 92.8 (C₅Me₅), 107.1 (RuCC), 117.8 (C1), 126.6 (t, 23 Hz, RuC), the following peaks correspond to the phenyl groups 127.3 (m), 127.4 (m), 128.9 (p), 128.7 (p), 133.3 (o), 133.5 (o), 137.0 (d, 48 Hz, i), 138.8 (m, i). Found: C, 58.1; H, 6.2%. RuC₄₀H₄₈P₂B₈ requires: C, 61.7; H, 6.2%. Accurate Mass, ES(+)-MS (*m/z*): 779.31600 Calculated for [Ru(C≡CC₂B₈H₉)(dppe)Cp*] + H], 779.31684.

Preparation of [Ru(1-C≡C-1,12-C₂B₁₀H₁₁)(dppe)Cp*] (3b). From [RuCl(dppe)Cp*] (160 mg, 0.224 mmol), **1b** (60 mg, 0.249 mmol), and KF (25 mg, 0.431 mmol) (2 h reflux), **3b** was obtained as yellow crystals (117 mg, 67%). IR (KBr disc, cm⁻¹): 3080w cage CH, 3058w phenyl CH, 2970w, 2912w, 2856w aliphatic CH, 2605s BH, 2081s C≡C, 1433 m, 1093 m, 699s, 533s. ¹H{¹¹B} NMR (CDCl₃): δ 1.48 (s, 15H, Me), 1.82 (s, 5H, B2-6H), 2.08 (m, 2H, CH₂), 2.14 (s, 5H,

B7-11H), 2.28 (s, 1H, C12H), 2.53 (m, 2H, CH₂), 7.10 (m, 4H, Ph), 7.24 (m, 6H, Ph), 7.40 (m, 6H, Ph), 7.59 (m, 4H, Ph). ³¹P{¹H} NMR (CDCl₃): δ 81.3 (s). ¹¹B NMR (CDCl₃): δ -11.1 (d, 5B, J_{BH} = 164 Hz, B2-6), -16.3 (d, 5B, J_{BH} = 164 Hz, B7-11). ¹³C{¹H} NMR: δ 9.8 (Me), 29.1 (m, CH₂), 53.4 (C12), 78.7 (C1), 92.6 (C₅Me₅), 103.7 (RuCC), 119.1 (t, 24 Hz, RuC), the following peaks correspond to the phenyl groups 127.3 (m), 127.4 (m), 128.8 (p), 133.1 (o), 133.3 (o), 136.9 (d, 47 Hz, i), 138.5 (m, i). Found: C, 56.5; H, 6.1%. RuC₄₀H₅₀P₂B₁₀ requires: C, 59.9; H, 6.3%. Accurate Mass, ES(+)-MS (*m/z*): 803.35103 Calculated for [Ru(C≡CC₂B₁₀H₁₁)(dppe)Cp*] + H], 803.35214.

Preparation of [Ru(dppe)Cp*]₂(μ -1,10-(C≡C)₂-1,10-C₂B₈H₈) (4a). From [RuCl(dppe)Cp*] (200 mg, 0.3 mmol), **2a** (51 mg, 0.16 mmol), and KF (30 mg, 0.5 mmol) (6 h reflux), **4a** was obtained (139 mg, 65%). IR (KBr disc, cm⁻¹): 3054w phenyl CH, 2962w, 2912w, 2860w aliphatic CH, 2592s BH, 2082s C≡C, 1432 m, 1095 m, 697s, 532s. ¹H{¹¹B} NMR (CDCl₃): δ 1.51 (s, 30H, Me), 1.70 (s, 8H, BH), 2.03 (m, 4H, CH₂), 2.68 (m, 4H, CH₂), 7.14, 7.17, 7.21 (m, 32H, Ph), 7.73 (m, 8H, Ph). ³¹P{¹H} NMR (CDCl₃): δ 80.6 (s). ¹¹B NMR (CDCl₃): δ -13.4 (d, 163 Hz). ¹³C{¹H} NMR (CDCl₃): δ 10.0 (Me), 29.5 (m, CH₂), 92.7 (C₅Me₅), 99.3 (C1), 106.8 (RuCC), 122.0 (t, 26 Hz, RuC), the following peaks correspond to the phenyl groups 127.2 (m), 127.3 (m), 128.7 (p), 128.8 (p), 133.3 (o), 133.6 (o), 137.1 (d, 47 Hz, i), 138.7 (m, i). Found: C, 62.0; H, 5.9%. Ru₂C₇₈H₈₈P₄B₈ requires: C, 65.2; H, 6.0%. Accurate Mass, ES(+)-MS (*m/z*): 1437.47037 Calculated for [Ru(dppe)Cp*]₂(μ -1,10-(C≡C)₂-1,10-C₂B₈H₈) + H], 1437.46796.

Preparation of [Ru(dppe)Cp*]₂(μ -1,12-(C≡C)₂-1,12-C₂B₁₀H₁₀) (4b). From [RuCl(dppe)Cp*] (100 mg, 0.149 mmol), **2b** (25 mg, 0.075 mmol), and KF (35 mg, 0.603 mmol) (3 h reflux) **4b** was obtained and crystallized from benzene (84 mg, 77%). IR (KBr disc, cm⁻¹): 3051w phenyl CH, 2962w, 2898w, 2856w aliphatic CH, 2597s BH, 2077s C≡C, 1433 m, 1094 m, 695s, 531s, 419s. ¹H{¹¹B} NMR (CDCl₃): δ 1.43 (s, 30H, Me), 1.96 (s, 10H, BH), 2.04 (m, 4H, CH₂), 2.51 (m, 4H, CH₂), 7.05 (m, 8H, Ph), 7.22 (m, 12H, Ph), 7.36 (m, 12H, Ph), 7.54 (m, 8H, Ph). ³¹P{¹H} NMR (CDCl₃): δ 80.4 (s). ¹¹B NMR (CDCl₃): δ -12.2 (d, 160 Hz). ¹³C{¹H} NMR (C₆D₆): δ 10.1 (Me), 29.5 (m, CH₂), 69.3 (C1), 92.7 (C₅Me₅), 104.5 (RuCC), 114.2 (t, 25 Hz, RuC), the following peaks correspond to the phenyl groups 127.6 (m), 129.2 (p), 133.5 (o), 133.8 (o), 137.5 (m, i), 139.2 (m, i). Found: C, 60.7; H, 6.0%. Ru₂C₇₈H₈₈P₄B₁₀ requires: C, 64.2; H, 6.1%. Accurate Mass, ES(+)-MS (*m/z*): 1461.50611 Calculated for [Ru(dppe)Cp*]₂(μ -1,12-(C≡C)₂-1,12-C₂B₁₀H₁₀) + H], 1461.50401.

Crystallography. Diffraction data were collected at 120K on a Bruker SMART 6000 (**3b**, **4a,b**), SMART 1K (**3a**) and Bruker Proteum-M (**1a**) diffractometers, using graphite-monochromated Mo-K α radiation. The structures were solved by direct-methods and refined by full matrix least-squares against *F*² of all data using *SHELXTL* software.³⁶ All non-hydrogen atoms were refined in anisotropic approximation except the disordered ones, H atoms were placed into the calculated positions and refined in “riding” mode. Molecule **4b** is located in the special position at the center of symmetry. Crystal of **4b** contains three independent solvent molecules of benzene; two of them are severely disordered. Crystallographic data for the structural analyses have been deposited with the Cambridge Crystallographic Data Centre, CCDC Nos. 637465–637469 for compounds **1a**, **3a**, **3b**, **4a** and **4b**, respectively. Copies of this information may be obtained free of charge from The Director, CCDC 12 Union Rd, Cambridge, CB2 1EZ, UK.

Computational Details. All computations were carried out with the Gaussian 03 package,³⁷ at the MPW1K/3-21G* level of theory.³¹ Frequency calculations on the resulting optimized geometries showed

(33) Bruce, M. I.; Ellis, B. G.; Low, P. J.; Skelton, B. W.; White, A. H. *Organometallics* **2003**, *22*, 3184.
 (34) (a) Connelly, N. G.; Geiger, W. E. *Chem. Rev.* **1996**, *96*, 877. (b) Rigaut, S.; Perruchon, J.; Guesmi, S.; Fave, C.; Touchard, D.; Dixneuf, P. H. *Eur. J. Inorg. Chem.* **2005**, 447.
 (35) Krejčík, M.; Daněk, M.; Hartl, F. J. *Electroanal. Chem.* **1991**, *317*, 179.

(36) (a) *SAINT*, v. 6.45; Bruker-AXS Inc.: Madison, Wisconsin, U.S.A., 2001. (b) *SADABS*, v.2006/1; Bruker-AXS Inc.: Madison, Wisconsin, U.S.A., 2006. (c) *SHELXTL*, v. 6.14; Bruker-AXS Inc.: Madison, Wisconsin, U.S.A. 2000.
 (37) Frisch, M. J.; et al. *Gaussian 03*, Revision C.02; Gaussian, Inc.: Wallingford, CT, 2004.

no imaginary frequencies. A scaling factor of 0.92 was applied to the calculated IR frequencies.²⁹ Electronic structure calculations and TD-DFT calculations were also carried out at the same level of theory. The rotation barriers between the two Ru(PH₃)₂Cp groups in **4a-H**, [4a-H]⁺, [4a-H]²⁺(LS) and [4a-H]²⁺(HS) were estimated by fixing the dihedral angles P1–Ru1–Ru2–P3 (Figure 4) at 15° intervals.

Acknowledgment. P.J.L. and M.A.F. thank the EPSRC for generous financial support. B.L.G. and J.F.H. thank the Pôle de Calcul Intensif de l'Ouest (PCIO) of the University of Rennes and the Institut de Développement et de Ressources en Informatique Scientifique (IDRIS-CNRS) for computing facilities. R.L.R. held a PhD scholarship from the University of Durham, Department of Chemistry Doctoral Training Account. These studies were facilitated by travel grants from the Royal Society, UK (P.J.L., J.F.H., F.H.) and the CNRS, France (J.F.H., P.J.L.).

Supporting Information Available: Full details of the preparation of **1a**, representative plots of the cyclic and square-wave voltammograms for **4a** and **4b**, full details of the computational methods employed, tables giving optimized geometries of **1a**, **1b**, **2a** and **2b**, absolute and relative energies of minima at the MPW1K/3-21G* level of theory, the orbital order and composition (%) of selected orbitals, excitation energies and oscillator strengths from TD-DFT computations for [3a-H]ⁿ⁺ (*n* = 0, 1), [3b-H]ⁿ⁺ (*n* = 0, 1), [4a-H]ⁿ⁺ (*n* = 0, 1, 2) and [4b-H]ⁿ⁺ (*n* = 0, 1, 2), tables of the absolute and relative energies of several minima found at the B3LYP/3-21G* level of theory, comparison of selected bond lengths for optimized geometries of **4b-H** at various levels of theory, and complete references 2a and 37.

JA0779755